Vector boson scattering at the LHC: counting experiments for unitarized models in a full six fermion approach

Alessandro Ballestrero,[a] **Diogo Buarque Franzosi,**[a,b] **Luisa Oggero**[b,c] **and Ezio Maina**[a,b]

[a]*INFN, Sezione di Torino,*
Via Giuria 1, 10125 Torino, Italy

[b]*Dipartimento di Fisica Teorica, Università di Torino,*
Via Giuria 1, 10125 Torino, Italy

[c]*Albert-Ludwigs-Universität Freiburg, Physikalisches Institut,*
D-79104 Freiburg, Germany

E-mail: ballestrero@to.infn.it, buarque@to.infn.it,
luisa.oggero@physik.uni-freiburg.de, maina@to.infn.it

ABSTRACT: Unitarization models describe phenomenologically the high energy behaviour of a strongly interacting symmetry breaking sector. In this work, predictions of some unitarized models in vector boson scattering at LHC are studied and compared with analogous studies in Equivalent Vector Boson Approximation and previous results for the benchmark no-Higgs scenario. To perform such studies, unitarized model amplitudes have been implemented in the PHANTOM Monte Carlo in a complete calculation with six fermions in the final state.

Contents

1   Introduction

ATLAS [1] and CMS [2] have recently presented the combination of all their Standard Model Higgs searches with the full 2011 dataset. Both experiments have registered a tantalizing excess of events at about 125 GeV with respect to the hypothesis of the absence of the Higgs. However the evidence is not yet sufficient to claim that the Higgs boson has been detected and statistical fluctuations might well explain the data. Therefore, the mechanism of ElectroWeak Symmetry Breaking (EWSB) remains unclear and the issue of high energy vector boson scattering continues to play a central role, either as the final test of the nature of the Higgs boson or, if the Higgs doesn't show up, as the main hunting ground for clues to alternative explanations. The vector vector scattering amplitudes grow

with energy when the bosons are longitudinally polarized and violate perturbative unitarity at about one TeV [3–8], requiring either the Higgs or some new physics in the energy range accessible to the LHC in order to tame this unphysical behaviour.[1]

Many alternative mechanisms of EWSB have been explored. We will not try to summarize the different models and simply refer to the literature. These theories typically predict the presence of new states which, much like the Higgs boson does, keep the scattering amplitudes small and the full theory amenable to a perturbative treatment. These additional particles, if light enough, could be observed at the LHC. If no such state is present, the scattering amplitudes become strong as the energy increases and perturbation theory breaks down. Moving beyond the perturbative approach it is possible to use Effective Field Theory (EFT) methods, in particular the Electroweak Chiral Lagrangian (EWChL) [13–19], to describe the low energy behaviour of the scattering amplitudes. The EWChL is a powerful approach for treating the low energy dynamics of systems with broken symmetries. It provides a systematic expansion of the full unknown Lagrangian in terms of the fields which are relevant at scales much lower than the symmetry breaking scale and does not require a detailed knowledge of the full theory. It is then possible to apply Unitarization Methods, using the lowest order terms in the scattering amplitudes as building blocks of all order expressions which respect unitarity and agree up to a finite order with the perturbative result.

Scattering processes among vector bosons have been scrutinized since a long time [20–34] with an increasing degree of sophistication. In a series of papers [35–38] we have analyzed all vector vector scattering channels, $4j\ell\nu$, $4j\ell^+\ell^-$, $2j3\ell\nu$, $2j\ell^+\ell^-\nu\bar{\nu}$, $2j\ell^\pm\ell^\pm\nu\nu$ and $2j4\ell$ ($\ell = e, \mu$) which are observable at the LHC, including all processes at order $\mathcal{O}(\alpha_{EM}^6)$, $\mathcal{O}(\alpha_{EM}^4\alpha_S^2)$ and $\mathcal{O}(\alpha_{EM}^2\alpha_S^4)$ as well as $t\bar{t}$+jets when appropriate. We have systematically compared a typical SM light Higgs scenario with the Higgsless case and with an example of Strongly Interacting Light Higgs (SILH) model [18].

In the last few years QCD corrections to boson-boson production via vector boson fusion [39–42] at the LHC have been computed and turn out to be below 10%. Recently, VBFNLO [43], a Monte Carlo program for vector boson fusion, double and triple vector boson production at NLO QCD accuracy, limited to the leptonic decays of vector bosons, has been released.

The first results for the NLO corrections to $W + 4j$ production have started to appear [44]. New techniques which exploit the angular distribution of vector boson decay products to determine the ratio of longitudinal and transverse polarization have been proposed in [45].

A number of papers [46–53] have explored the possibility that the increasing strength of the interaction between vector bosons as the energy of the scattering is augmented might lead to the formation of resonant states in analogy to Low Energy QCD in which the growth of the pion-pion scattering amplitude is regulated by the appearance of the ρ resonance. Most of these efforts have resorted to the EVBA, since strictly speaking the unitarization procedure is defined only for on-shell scattering amplitudes between longitudinally polarized vector bosons. This approach however suffers of all the well known deficiencies of the

---

[1]Detailed reviews and extensive bibliographies can be found in refs. [9–12].

EVBA and in particular neglects the contribution of transversely polarized vector bosons and all off-shell effects which can be sizable. The strong gauge cancellations between signal and irreducible background and the reliability of the Equivalent Vector Boson Approximation (EVBA) have been studied in [54]. A preliminary analysis in the EVBA of the observability of partial unitarization of longitudinal vector boson scattering in SILH models at the LHC can be found in ref. [55]. Unitarization models can describe the strongly interacting symmetry breaking sector, with or without formation of resonances. A recipe for embedding the unitarized amplitudes in the full, off-shell, $2 \to 6$ amplitude, which is necessary for a reliable description of VV scattering at the LHC, has been first proposed in refs. [56, 57] and later refined in ref. [58] and made available in WHIZARD [59].

In this paper we present the implementation of several unitarization schemes, the K-matrix, the Inverse Amplitude Method (IAM) and the N/D procedure, within the PHANTOM [60] Monte Carlo event generator along the lines of ref. [58]. The unitarized amplitudes are extended off-shell in a natural way and embedded in the framework of a complete six parton final state calculation. We then study the prospect of detecting signals of these unitarized models at the LHC taking into account all relevant backgrounds, including top-antitop production, possibly with additional jets, and vector boson plus four jets production.

The paper is organized as follows. In section 2 we present the basic formalism of the EFT approach and we introduce the unitarization schemes which are available in PHANTOM. In section 3 we compare the results obtained in a complete calculation with those obtained in the EVBA. Then, in section 4 we present the main results for all relevant decay modes of the final state bosons and finally we state our conclusions.

2 Implementation of unitarized models in PHANTOM

Pion-pion scattering has been for a long time described by effective Lagrangians. In this framework, when the energy increases, non perturbative effects of QCD dynamics are unavoidable as for example manifested in the appearance of new resonances. A purely phenomenological approach to describe this physics is given by Unitarization Models. They are based on *ad-hoc* formulas that force the amplitudes of Goldstone bosons scattering to satisfy the unitarity condition and maintain the low energy behavior. Unitarization models are intended to represent the approximate magnitude of these amplitudes beyond the low-energy regime and have been able in some cases to describe some resonances of QCD.

In view of the great similarities between low energy QCD and Electroweak physics, the ideas of unitarization models have been translated to a strong symmetry breaking sector in several studies [31, 46, 48, 50, 56–58]. They are not complete quantum field theories and in particular they typically violate crossing symmetry, but despite these deficiencies, unitarization models fulfill their phenomenological purpose of estimating the magnitude of strong VV scattering cross sections much beyond the range of validity of the effective theory.

In this section we describe the main aspects of the implementation of unitarization models in a complete six-fermion in the final state framework for the PHANTOM Monte Carlo generator.

2.1 The electroweak chiral Lagrangian and low energy amplitudes

If EWSB is driven by new strong dynamics at TeV scale, the EWChL (inspired by the Chiral Lagrangian of QCD) provides the most economical description of electroweak physics below this scale. The EWChL accounts for all particles of the SM apart from the Higgs boson. The gauge symmetry $SU(2)_L \times U(1)_Y$ is maintained by explicitly introducing the three Goldstone bosons, $\omega^a(x)$ with $a = 1, 2, 3$, gathered in an $SU(2)$ matrix field

$$\Sigma(x) = \exp\left(\frac{i\sigma^a \omega^a(x)}{v}\right), \tag{2.1}$$

where σ^a are the Pauli matrices and $v \approx 246\,GeV$ is the decay constant of the Goldstone boson that gives the right masses to vector bosons. Σ transforms under $SU(2)_L \times U(1)_Y$ as

$$\Sigma \to U_L(x)\Sigma U_Y^\dagger(x), \tag{2.2}$$

$$U_L(x) = \exp\left(\frac{i\beta^a(x)\sigma^a}{2}\right), \qquad U_Y(x) = \exp\left(\frac{i\beta_Y(x)\sigma^3}{2}\right). \tag{2.3}$$

The familiar pieces of the chiral Lagrangian, that emerge for example from the $M_H \to \infty$ limit of the SM, are:

$$\begin{aligned} \mathcal{L} =& \frac{v^2}{4}\,\text{Tr}[(D_\mu\Sigma)^\dagger(D^\mu\Sigma)] - \frac{1}{4}G_{\mu\nu}^a G^{\mu\nu,a} - \frac{1}{4}W_{\mu\nu}^i W^{\mu\nu,i} - \frac{1}{4}B_{\mu\nu}B^{\mu\nu} \\ & + i\,\bar{Q}_L\slashed{D}Q_L + i\,\bar{Q}_R\slashed{D}Q_R + i\,\bar{L}_L\slashed{D}L_L + i\,\bar{L}_R\slashed{D}L_R \\ & - (\bar{Q}_L\Sigma M_Q Q_R + \bar{L}_L\Sigma M_L L_R + \text{h.c.}). \end{aligned} \tag{2.4}$$

The first term has the form of a non-linear sigma model, which is non-renormalizable in four dimensions; therefore, a cut-off scale Λ must be set. Deviations from the SM in the absence of the Higgs boson can be parametrized in terms of a low energy expansion in E/Λ, consisting of operators of increasing dimension.

Besides the usual spontaneous breaking pattern of the SM, $SU(2)_L \times U(1)_Y \to U(1)_{\text{em}}$, experiment demands that the Higgs sector also approximately respects a larger, $SU(2)_L \times SU(2)_R$ symmetry, $\Sigma \to U_L\Sigma U_R^\dagger$, which is spontaneously broken to the diagonal subgroup $SU(2)_D$ (where $U_L = U_R$) by the VEV $\langle\Sigma\rangle = 1$. Only two dimension-4 operators which respect these symmetries are relevant for the study of Vector Boson Scattering (VBS), they are:

$$\mathcal{L}_4 = \alpha_4 \text{Tr}[V^\mu, V^\nu]^2, \tag{2.5}$$

$$\mathcal{L}_5 = \alpha_5 \text{Tr}[V_\mu, V^\mu]^2, \tag{2.6}$$

where $V_\mu \equiv (D_\mu\Sigma)\Sigma^\dagger$.

For the description of the elastic scattering of longitudinal bosons, we are going to make use of the Goldstone Boson (GB) amplitudes, which can be translated into the corresponding physical longitudinal boson scattering through the Goldstone Boson Equivalence Theorem (GBET) [6, 61–63]. The GBET states that an amplitude involving longitudinal vector bosons, V_L, is well approximated at high energy by the corresponding amplitude obtained by replacing V_L with the Goldstone bosons, ω, in any renormalizable R_ξ gauge.

Assuming isospin custodial symmetry, all $2 \to 2$ Goldstone boson scattering processes can be described by a single master amplitude, $A(s, t, u)$ which satisfies $A(s, t, u) = A(s, u, t)$. It can be identified as the amplitude of the $\omega^+ \omega^- \to zz$ process.

The lowest order term of the master amplitude in the E/Λ expansion, identified as the Low Energy Theorem (LET) [64] and reproduced by the non-linear sigma model term in the Lagrangian (first term in the r.h.s. of eq. (2.4)), is given by

$$A^{(1)}(s, t, u) = \frac{s}{v^2}. \tag{2.7}$$

At next-to-leading order in the E/Λ expansion, we must include the higher-dimension operators, eqs. (2.5)–(2.6), and one-loop diagrams. The NLO amplitude is given by [65]

$$A^{(2)}(s, t, u) = 4\alpha_4 \frac{t^2 + u^2}{v^4} + 8\alpha_5 \frac{s^2}{v^4} + \frac{1}{16\pi^2} \left[\frac{10s^2 + 13(t^2 + u^2)}{18v^4} + \frac{s^2}{2v^4} \ln\left(\frac{\mu^2}{-s}\right) \right.$$
$$\left. + \frac{t(s + 2t)}{6v^4} \ln\left(\frac{\mu^2}{-t}\right) + \frac{u(s + 2u)}{6v^4} \ln\left(\frac{\mu^2}{-u}\right) \right], \tag{2.8}$$

where μ is the renormalization scale. The infinities that appear when computing one loop diagrams are absorbed by defining renormalized parameters in the higher-dimension operators of the effective Lagrangian. The terms proportional to factors of the weak coupling, g, which do not grow asymptotically with s, will be recovered in the complete $2 \to 6$ implementation. For the moment, we just need the leading contribution from the longitudinal boson scattering.

The α_4 and α_5 parameters contribute to the T-parameter [66–68] and therefore are constrained by electroweak precision data [69, 70]. Stronger limits are obtained if quadratically divergent terms are taken into account [71]. Arguments based on unitarity and causality could also constrain these parameters [72]. In this case, the magnitude of α_4 and α_5 is required by data to be smaller than about 10^{-2}.

2.2 Unitarization of low energy amplitudes

In the EWChL framework, when E approaches Λ, the perturbative expansion starts to loose its predictive power. Moreover, low energy amplitudes of longitudinal vector boson scattering violate unitarity at much lower scales $E \approx 1.2\,\text{TeV}$. To describe the magnitude of the cross section much beyond the unitarity violation scale we can unitarize the low energy amplitudes.

In order to perform the unitarization procedure, it is convenient to expand the master amplitudes into isospin, I, eigenamplitudes according to[2]

$$A_0(s, t, u) = 3A(s, t, u) + A(t, s, u) + A(u, s, t), \tag{2.9a}$$

$$A_1(s, t, u) = A(t, s, u) - A(u, s, t), \tag{2.9b}$$

$$A_2(s, t, u) = A(t, s, u) + A(u, s, t). \tag{2.9c}$$

---

[2]These expressions as well as those in eq. (2.10) can be derived using the Clebsh-Gordan coefficients for the coupling of two $I = 1$ representation, exploiting the scalar nature of the interaction Hamiltonian. The pion states are defined as: $|\pi^+> = 1/\sqrt{2}(|\pi_1> + i |\pi_2>) = -|1, 1>$, $|\pi^0> = |\pi_3> = |1, 0>$, $|\pi^-> = 1/\sqrt{2}(|\pi_1> - i |\pi_2>) = |1, -1>$.

The individual scattering amplitudes can be expressed in terms of the isospin eigenamplitudes as follows:

$$A(\omega^+\omega^- \to zz) = \frac{1}{3}A_0(s,t,u) - \frac{1}{3}A_2(s,t,u)\,, \tag{2.10a}$$

$$A(\omega^+z \to \omega^+z) = \frac{1}{2}A_1(s,t,u) + \frac{1}{2}A_2(s,t,u)\,, \tag{2.10b}$$

$$A(\omega^+\omega^- \to \omega^+\omega^-) = \frac{1}{3}A_0(s,t,u) + \frac{1}{2}A_1(s,t,u) + \frac{1}{6}A_2(s,t,u)\,, \tag{2.10c}$$

$$A(\omega^+\omega^+ \to \omega^+\omega^+) = A_2(s,t,u)\,, \tag{2.10d}$$

$$A(zz \to zz) = \frac{1}{3}A_0(s,t,u) + \frac{2}{3}A_2(s,t,u)\,. \tag{2.10e}$$

Each isospin eigenamplitude is then expanded into partial waves of definite angular momenta, J, according to

$$A_{IJ}(s) = \frac{1}{2}\int_{-1}^{1} d\cos\theta\, P_J(cos\theta) A_I(s,t,u), \tag{2.11}$$

where $P_J(x)$ are the Legendre polynomials.

Notice for instance the behavior of the $I = 0$, $J = 0$ eigenamplitude:

$$A_{00}(s) = 2\frac{s}{v^2} + \left[\frac{8}{3}\left(7\alpha_4(\mu) + 11\alpha_5(\mu)\right) + \frac{1}{16\pi^2}\left(2\ln\left(\frac{\mu^2}{-s}\right) + \frac{7}{9}\ln\left(\frac{\mu^2}{s}\right) + \frac{11}{54}\right)\right]\frac{s^2}{v^4}. \tag{2.12}$$

The absorptive part of this amplitude is extracted by setting $\ln(-s) = \ln s - i\pi$, when $s > 0$ and it reproduces the perturbative unitarity relation

$$\mathrm{Im}\, A_{IJ}^{(2)}(s) = \frac{1}{32\pi}|A_{IJ}^{(1)}(s)|^2\,, \tag{2.13}$$

where $A^{(1)}(s)$ is the lowest order amplitude (the first term of the r.h.s. of eq. (2.12)) and $A^{(2)}(s)$ is the NLO part given by the term proportional to s^2/v^4. This amplitude presents, up to one loop, the correct singularity structure, crossing property and chiral symmetry. Nonetheless, this is not sufficient to guarantee a well behaved cross section at high energies such as those of the LHC.

Therefore, each individual isospin-spin eigenamplitude must be unitarized over the whole spectrum employing a specific protocol. We have implemented the three most popular models of unitarization: the K-matrix scheme (KM), the Inverse Amplitude Method (IAM) and the N/D protocol. The main purpose of these schemes is to transform the isospin-spin eigenamplitudes, $A_{IJ}(s)$, into new expressions, $\hat{A}_{IJ}(s)$, which simultaneously respect the unitarity condition,

$$\mathrm{Im}\, \hat{A}_{IJ}(s) = \frac{1}{32\pi}|\hat{A}_{IJ}(s)|^2\,, \tag{2.14}$$

and have the appropriate low energy behavior,

$$\hat{A}_{IJ}(s) \xrightarrow{s\to 0} A_{IJ}(s)\,. \tag{2.15}$$

2.2.1 K-matrix scheme

The unitarized amplitude through the K-Matrix scheme is given by

$$\hat{A}_{IJ}^{KM}(s) = \frac{32\pi}{32\pi \operatorname{Re}\left(1/A_{IJ}(s)\right) - i}\,. \tag{2.16}$$

This expression exactly satisfies elastic unitarity. As an example, let us take the pure Low Energy Theorem expression, $A_{00}(s) = 2s/v^2$. The KM procedure transform this expression into

$$\hat{A}_{00}^{KM}(s) = \frac{2s}{v^2}\frac{1}{\left(1 - \frac{i}{16\pi v^2}s\right)} \xrightarrow{s\to\infty} 32\pi i\,, \tag{2.17}$$

which instead of growing quadratically with energy, asymptotically approaches unitarity saturation.

We have also implemented in the code the possibility of incorporating the exchange of heavy resonances of definite angular momentum, J, and isospin, I, unitarized by the K-Matrix scheme. We have followed the prescription given in [58], adding new degrees of freedom to incorporate resonances coupled to the Goldstone bosons. This unitarization procedure normally reproduces resonances with s-dependent widths.

2.2.2 N/D protocol

Besides violating crossing symmetry, the KM unitarization procedure spoils the singularity structure of the fixed-order amplitudes. It fixes the absorptive part for $s > 0$ guaranteeing unitarity at arbitrary energy at the cost of ruining the left-hand cut. In the N/D protocol, unitarity is exactly restored with the extra quality of improved analytical properties. In the N/D method, each partial wave amplitude is expressed as the quotient of two functions,

$$\hat{A}_{IJ}^{N/D}(s) = \frac{N_{IJ}(s)}{D_{IJ}(s)}\,. \tag{2.18}$$

The denominator function, $D(s)$, contains the right hand cut (or unitarity cut) while the left-hand cut is incorporated in the numerator function, $N(s)$.

In eq. (2.12) for instance the left hand cut first appears through the term $(7/9)\ln(\mu^2/s)$ which acquires an imaginary part for $s < 0$. To unitarize the amplitudes and simultaneously reproduce the left hand cut of eq. (2.12), at one loop precision, we follow the prescription given by [49]. We define

$$G(s) = \frac{1}{32\pi^2}\ln\left(-\frac{s}{M^2}\right)\,, \tag{2.19}$$

where M is a new free parameter. The unitarized amplitudes take the form

$$N_{IJ}(s) = A_{IJ}^{(1)}(s) + A_{IJ}^{(2)}(s) + G(s)(A_{IJ}^{(1)}(s))^2\,; \tag{2.20}$$

$$D_{IJ}(s) = 1 + G(s)N_{IJ}(s)\,. \tag{2.21}$$

The terms $A_{IJ}^{(1)}(s)$ are originated from the lowest order amplitude, eq. (2.7), while the $A_{IJ}^{(2)}(s)$ are originated from the NLO terms, eq. (2.8). $N_{IJ}(s)$ bears exclusively the left hand cut, which is kept at the unitarized amplitude, $\hat{A}_{IJ}^{N/D}(s)$, at the one-loop level precision. For $s > 0$, $N_{IJ}(s)$ is real and the unitarity cut is completely provided by the denominator function, $D_{IJ}(s)$, making $\hat{A}_{IJ}^{N/D}(s) = \frac{N_{IJ}(s)}{D_{IJ}(s)}$ to exactly respect the unitarity condition, eq. (2.14).

2.2.3 Inverse amplitude method

In the Inverse Amplitude Method (IAM), isospin-spin eigenamplitudes are unitarized by the following prescription:

$$\hat{A}_{IJ}^{IAM}(s) = \frac{A_{IJ}^{(1)}(s)}{1 - A_{IJ}^{(2)}(s)/A_{IJ}^{(1)}(s)}. \tag{2.22}$$

It can be shown that eq. (2.22) is a special case of the N/D method, it maintains the proper analytical structure with the correct branch cuts. In addition, for certain values of the chiral coefficients, α_4 and α_5, the unitarized amplitudes, both by N/D and IAM protocols, present poles that can be interpreted as dynamically generated resonances.

This method has been widely and succefully applied in pion-pion and pion-kaon scattering, in many cases reproducing lightest resonances.

2.3 Implementing unitarized models in six parton final states within `PHANTOM`

No detailed phenomenological study has been performed in the context of unitarization models in a complete calculation. In most cases, previous results have relied on the Effective Vector Boson Approximation (EVBA), which is known to produce inaccurate predictions for VBS at high energy. With a complete $2 \to 6$ calculation, all diagrams are summed coherently, interference terms and off-shell effects are completely accounted for. The contribution of transversely polarized bosons is also correctly included. A detailed description of the implementation of K Matrix unitarized model in `WHIZARD` and some examples of simulation with the full 6 fermion calculation is given in ref. [59].

It is important to notice that the LET part is already present in the complete tree-level calculation. In order to avoid double counting it is necessary to define a correction to the on-shell amplitudes, given by

$$\Delta A_{IJ}(s) = \hat{A}_{IJ}(s) - A_{IJ}^{(1)}(s). \tag{2.23}$$

These corrections to the isospin-spin eigenamplitudes are translated back into isospin eigenamplitudes according to

$$\Delta A_I(s,t) = \sum_J (2J+1)\Delta A_{IJ}(s)P_J(\cos\theta). \tag{2.24}$$

For our purposes, it is enough to truncate the series at $J = 2$. Finally, the isospin eigenamplitudes are translated into corrections to the individual scattering amplitudes according to eq. (2.10).

We have for example:

$$\Delta A(\omega^+\omega^- \to zz) = 8\left[\frac{v^4}{24s^2}\left(\Delta A_{00}(s) - \Delta A_{20}(s)\right) - \frac{5v^4}{12s^2}\left(\Delta A_{02}(s) - \Delta A_{22}(s)\right)\right]\frac{s^2}{v^4}$$
$$+ 4\left[\frac{5v^4}{4s^2}\left(\Delta A_{02}(s) - \Delta A_{22}(s)\right)\right]\frac{t^2+u^2}{v^4}. \tag{2.25}$$

In order to introduce each of these on-shell elastic scattering amplitudes into the complete $2 \to 6$ matrix elements, a method based on the definition of new quartic vertexes has been suggested in [56, 57] and further developed in [58]. Our implementation of this approach in the PHANTOM Monte Carlo generator is briefly explained in the following.

2.3.1 New quartic vertexes

In unitary gauge the quartic gauge interactions of massive vector bosons can be extracted from the EWChL, eqs. (2.4)–(2.6), with $\Sigma = 1$:

$$
\begin{aligned}
\mathcal{L}_{QGC} =& g^2 \cos^2 \theta_{\mathrm{w}} \left[g_1^{ZZ} Z^\mu Z^\nu W_\mu^- W_\nu^+ - g_2^{ZZ} Z^\mu Z_\mu W^{-\nu} W_\nu^+ \right] \\
& + \frac{g^2}{2} \left[g_1^{WW} W^{-\mu} W^{+\nu} W_\mu^- W_\nu^+ - g_2^{WW} \left(W^{-\mu} W_\mu^+ \right)^2 \right] \\
& + \frac{g^2}{4 \cos^4 \theta_{\mathrm{w}}} h^{ZZ} (Z^\mu Z_\mu)^2 .
\end{aligned}
\tag{2.26}
$$

Considering only the $\mathcal{L}_4$ and $\mathcal{L}_5$ extra terms, eqs. (2.5)–(2.6), the values of the couplings are given by [59]

$$
\begin{aligned}
g_1^{ZZ} &= 1 + \frac{g^2}{\cos^4 \theta_{\mathrm{w}}} \alpha_4 , & g_2^{ZZ} &= 1 - \frac{g^2}{\cos^4 \theta_{\mathrm{w}}} \alpha_5 , \\
g_1^{WW} &= 1 + g^2 \alpha_4 , & g_2^{WW} &= 1 - g^2 (\alpha_4 + 2\alpha_5) , \\
h^{ZZ} &= g^2 (\alpha_4 + \alpha_5) .
\end{aligned}
\tag{2.27}
$$

In the SM, $g_i^{VV} = 1$ and $h^{ZZ} = 0$, where $i = 1, 2$ and $VV = WW, ZZ$.

As already mentioned, the unitarization procedures used herein violate crossing symmetry, therefore, it is not possible to write a Lagrangian for the model and to derive the corresponding vertexes in a general form. Instead, it is necessary to identify first which kind of vector vector scattering processes are embedded in the complete $2 \to 6$ set of Feynman diagrams. As a second step the vertexes are appropriately modified. The possible scattering reactions, $W^+W^- \to W^+W^-$, $W^+W^- \to ZZ$, $W^\pm W^\pm \to W^\pm W^\pm$, can be identified from the flow of fermion external momenta.

For each scattering type, the quartic vertex is modified in such a way to reproduce the full on-shell scattering amplitudes. They can be written in the form:

$$
V(Z^\mu Z^\nu W^{-\rho} W^{+\sigma}) = -ig^2 \cos^2 \theta_{\mathrm{w}} [2k_1^{ZW} g^{\mu\nu} g^{\rho\sigma} - k_2^{ZW} g^{\mu\sigma} g^{\nu\rho} - k_3^{ZW} g^{\mu\rho} g^{\nu\sigma}], \tag{2.28a}
$$

$$
V(W^{-\mu} W^{+\nu} W^{-\rho} W^{+\sigma}) = ig^2 [2k_1^{WW} g^{\mu\rho} g^{\nu\sigma} - k_2^{WW} g^{\mu\sigma} g^{\nu\rho} - k_3^{WW} g^{\mu\nu} g^{\rho\sigma}], \tag{2.28b}
$$

$$
V(Z^\mu Z^\nu Z^\rho Z^\sigma) = ig^2 \frac{2}{\cos^4 \theta_{\mathrm{w}}} [k_1^{ZZ} g^{\mu\nu} g^{\rho\sigma} + k_2^{ZZ} g^{\mu\sigma} g^{\nu\rho} + k_3^{ZZ} g^{\mu\rho} g^{\nu\sigma}], \tag{2.28c}
$$

where the k_i coefficients are form factors which depend on the particular vector vector scattering process. For example for $ZZ \to W^+W^-$ we have:

$$
k_1^{ZW} = 1 - \frac{g^2}{\cos^4 \theta_{\mathrm{w}}} \left[\frac{v^4}{24s^2} (\Delta A_{00}(s) - \Delta A_{20}(s)) - \frac{5v^4}{12s^2} (\Delta A_{02}(s) - \Delta A_{22}(s)) \right], \tag{2.29a}
$$

$$
k_2^{ZW} = k_3^{ZW} = 1 + \frac{g^2}{\cos^4 \theta_{\mathrm{w}}} \left[\frac{5v^4}{4s^2} (\Delta A_{02}(s) - \Delta A_{22}(s)) \right]. \tag{2.29b}
$$

scenario	$\alpha_4(1\text{TeV})$	$\alpha_5(1\text{TeV})$
A	0.0	0.003
B	0.002	-0.003
D	0.008	0.0

Table 1. Parameters for the IAM models.

Notice that for on-shell VBS, these new vertexes reproduce the unitarized amplitudes (e.g. eq. (2.25)) at high energies. Since $\epsilon_L^\mu \xrightarrow{E \gg M_V} \frac{p^\mu}{M_V}$, in the high energy limit the Mandelstam variables of the scattering can be reexpressed in terms of the vector longitudinal polarizations in the form:
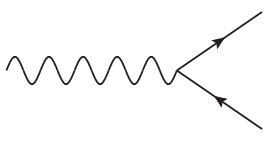
$$s^2 = 2p_1 \cdot p_2 \, 2p_3 \cdot p_4 \approx 4M_{V_1} M_{V_2} M_{V_3} M_{V_4} \, g_{\mu\nu} g_{\rho\sigma} \, \epsilon_1^\mu \epsilon_2^\nu \epsilon_3^\rho \epsilon_4^\sigma, \qquad (2.30\text{a})$$

$$t^2 = 2p_1 \cdot p_3 \, 2p_2 \cdot p_4 \approx 4M_{V_1} M_{V_2} M_{V_3} M_{V_4} \, g_{\mu\rho} g_{\nu\sigma} \, \epsilon_1^\mu \epsilon_2^\nu \epsilon_4^\rho \epsilon_4^\sigma, \qquad (2.30\text{b})$$

$$u^2 = 2p_1 \cdot p_4 \, 2p_2 \cdot p_3 \approx 4M_{V_1} M_{V_2} M_{V_3} M_{V_4} \, g_{\mu\sigma} g_{\nu\rho} \, \epsilon_1^\mu \epsilon_2^\nu \epsilon_3^\rho \epsilon_4^\sigma, \qquad (2.30\text{c})$$

where the subindexes 1, 2 indicate the two incoming bosons and 3, 4 the two outgoing ones. M_V are the masses of the bosons, either M_W or M_Z. With this identification, the corrected amplitudes take exactly the form of quartic vertexes contracted with external polarization vectors. The difference with respect to the complete six-fermions final state calculation is that the role of the polarization vectors in eq. (2.30) is played by the sub-diagrams with the final state fermions and the boson propagators,

$$\epsilon^\mu = \qquad\qquad\qquad\qquad . \qquad\qquad (2.31)$$

At low energies, the corrections ΔA_{IJ} tend to vanish; therefore, the complete calculation is recovered. For high energies, the typical growth of longitudinal vector boson scattering is moderated by the ΔA_{IJ} corrections reproducing the unitarized elastic scattering of the GB, which is a good approximation to the scattering of the longitudinal modes at high energy according to the Goldstone Boson Equivalence Theorem.

3 Comparison with EVBA results

The results of our implementation have been compared with those obtained in ref. [50] by Butterworth, Cox and Forshaw, where an on-shell calculation based on the Effective W Approximation has been employed. Three instances of the Inverse Amplitude Method, eq. (2.22), have been considered. They differ in the choice of the α_4 and α_5 coefficients as reported in table 1. The renormalization scale has been set at $\mu=1$ TeV.

The IAM procedure gives rise to poles in the unitarized amplitudes which can be interpreted as resonances whose mass and width are given by eq. (3.1) for the vector

Generation cuts
$p_T(\ell^{\pm}) > 20$ GeV
$|\eta(\ell^{\pm})| < 3.0$
$p_T(j) > 30$ GeV
$|\eta(j)| < 6.5$
$M(jj) > 60$ GeV
$M(\ell^+\ell^-) > 20$ GeV

Table 2. Standard acceptance cuts applied in the event generation and present in all results of this section. Here $j = d, u, s, c, b, g$.
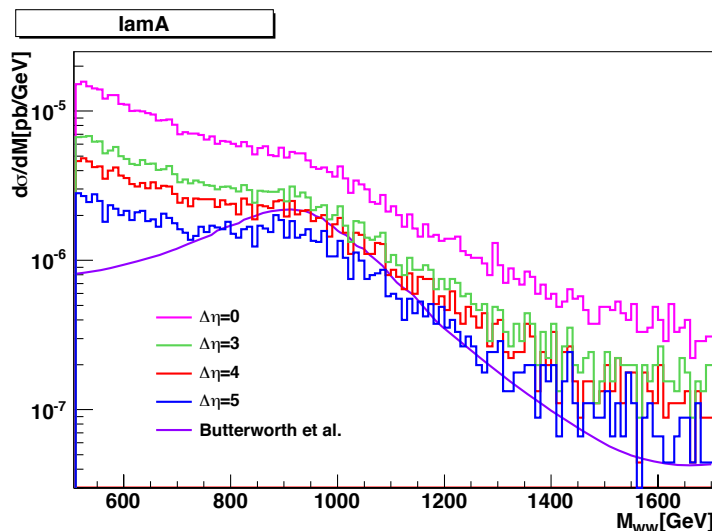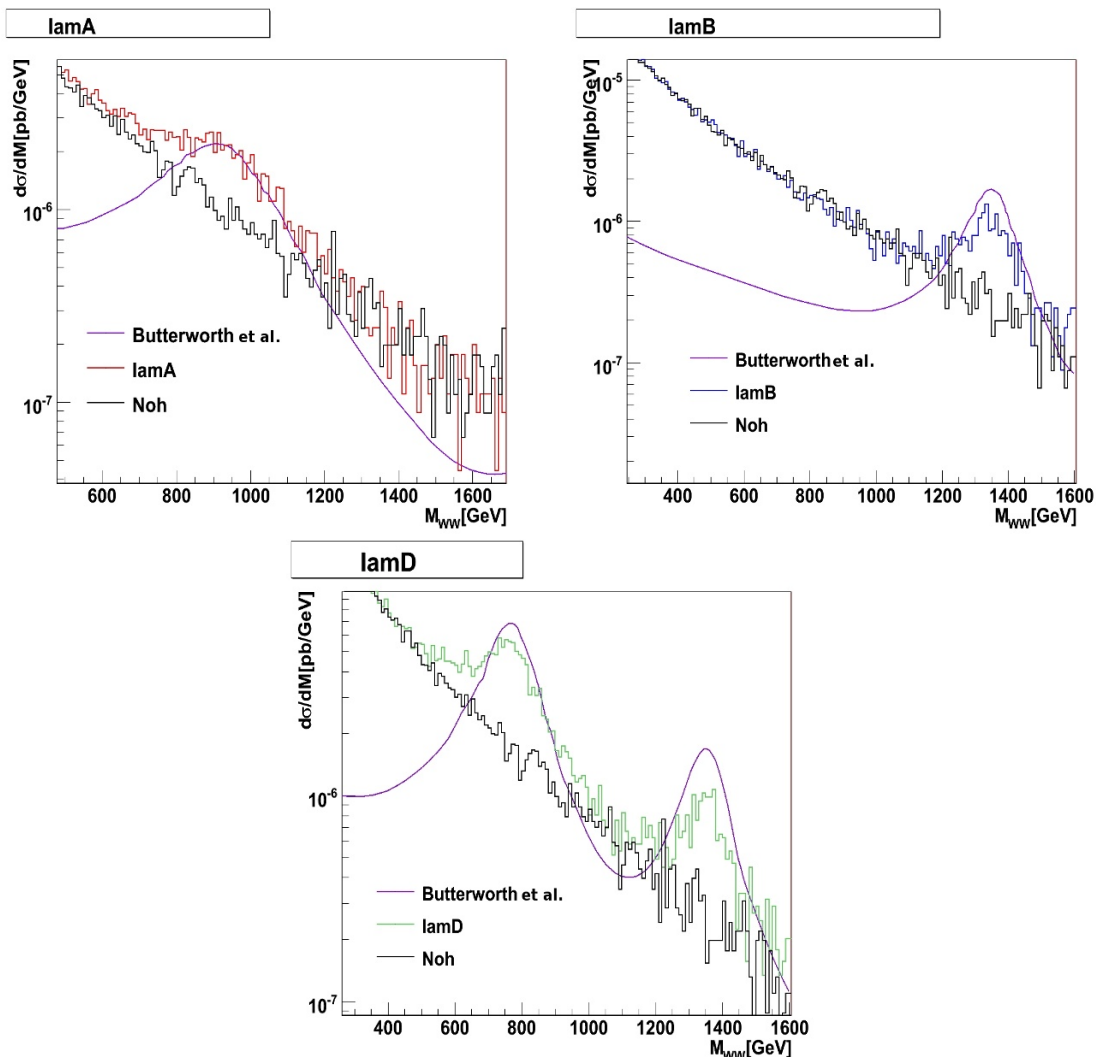

Figure 1. Comparison between the $M(WW)$ distribution in $PP \to 2j\mu^{\pm}e^{\mp}\nu\bar{\nu}$ in the complete calculation and the EVBA calculation in ref. [50] (in purple) multiplied by the appropriate branching ratio, $BR = 2/81$, for the IAM A model. The complete calculation is shown with different cuts in pseudo-rapidity. Processes with external b-quarks have been discarded.

channel $I = 1$, $J = 1$ and by eq. (3.2) for the scalar case $I = 0$, $J = 0$. Scenario A presents a scalar resonance at about 1 TeV, scenario B a vector resonance at about 1.4 TeV, and scenario D a scalar resonance at 0.8 TeV and a vector one at 1.4 TeV.

$$M_V^2 = \frac{v^2}{4(\alpha_4 - 2\alpha_5) + \frac{1}{9(4\pi)^2}}, \qquad \Gamma_V = \frac{M_V^3}{96\pi v^2}. \qquad (3.1)$$

$$M_S^2 = \frac{12v^2}{16(11\alpha_5(M_S) + 7\alpha_4(M_S)) + \frac{101}{3(4\pi)^2}}, \qquad \Gamma_S = \frac{M_S^3}{16\pi v^2}. \qquad (3.2)$$

We have computed the complete set of purely electroweak processes for the $2j\mu^{\pm}e^{\mp}\nu\bar{\nu}$ final state, with the generation cuts in table 2. A big contribution to these final states

Figure 2. Comparison between the $M(WW)$ distribution in $PP \to 2j\mu^{\pm}e^{\mp}\nu\bar{\nu}$ for the IAM A (*at top left*), IAM B (*at top right*) and IAM D (*bottom*) models obtained with a complete calculation with $\Delta\eta > 4$ and the predictions from ref. [50] multiplied by the appropriate branching ratio, $BR = 2/81$.

comes from electroweak $t\bar{t}$ production. Therefore, in order to avoid this contamination in the comparison, we have considered only processes without bottom quarks in the initial or final state. Moreover, different cuts in the pseudo-rapidity difference between tag jets have been tested in order to enhance the scattering contribution.

The VV invariant mass distribution in the IAM A model is presented in figure 1. It shows the prediction of the complete calculation, as implemented in PHANTOM, and the corresponding cross section derived in ref. [50] in the EVBA. The data points for the EVBA results have been extracted from the figures of ref. [50] and rescaled by the branching ratio for $W^{+}W^{-} \to \mu^{\pm}e^{\mp}\nu\bar{\nu}$, $BR = 2/81$, since the W decays were not included. For the

complete calculation, four different cuts on the difference in pseudorapidity between jets, $\Delta\eta(jj) > 0, 3, 4, 5$, have been applied. As expected the resonance peak is more clearly seen at larger separation between tag jets.

It can be observed that the curve with $\Delta\eta > 4$ is well reproduced by the approximation in ref. [50] close to the peak at about one TeV. Outside this regions the curve of ref. [50] underestimate by a large amount the actual cross section. The comparison between the present results and those obtained in EVBA should not be taken too literally. In EVBA the final state jets have been completely integrated over and therefore no separation cut between tag jets can be applied. While the approximate total cross section obtained is in rough agreement with the full calculation in the peak region, too many details would be missing in a simulation based on the EVBA to allow for a realistic study of the experimental observability of these processes.

In figure 2 we show the comparison for all three scenarios. As before, $\Delta\eta > 4$ and no process with external b-quarks is included. Again, large discrepancies can be observed outside the peak region. We also present in black the result for the no-Higgs scenario. It is interesting to notice that the unitarized models and the no-Higgs scenario are in reasonable agreement outside of the resonance peak in the considered mass range. We will comment further on this point when dicussing the different final states in section 4.

4 Counting experiments for unitarized models at LHC

In this section, a number of phenomenological studies at the LHC for some typical choice of unitarization schemes and parameters are presented. We limit our analyses to the design energy of 14 TeV and we do not attempt to determine the parameter range for which resonances in the new scenarios can be experimentally discovered. For some final states and for scalar resonances, looking for new resonances is just an extension of Standard Model Higgs searches. For different kind of resonances however a completely different strategy might be required. We will therefore examine in which cases there will be a significant excess of events at high invariant mass and if it will be possible to detect it at the LHC. For this reason we give to these searches the name of counting experiments. All our results are at parton level only, and must be considered as a first indication of the effects of unitarized models in the context of a complete lowest order calculation which avoids the EVBA and takes all relevant irreducible backgrounds into account.

In addition to the cases already considered in the previous section (IAM A, IAM B and IAM D) we will consider the following scenarios:

- IAM C: it is another Inverse Amplitude Method unitarization model with parameters $\alpha_4 = 0.002$ and $\alpha_5 = -0.001$. This model produces a vector resonance at about 1.9 TeV. It was already discussed in ref. [50].

- N/D A: uses the N/D unitarization method with M = 1 TeV, $\alpha_4 = 0$ and $\alpha_5 = 0.003$. It presents a 1 TeV scalar resonance as in the IAM A model but with a softer resonance peak. Notice however that in general the N/D method gives models which can be quite different from the other methods we have considered.

Basic Cuts
$p_T(\ell^\pm) > 20$ GeV
$|\eta(\ell^\pm)| < 3.0$
$M(\ell^+\ell^-) > 20$ GeV
$M(\ell^+\ell^-) > 250$ GeV $(2jW^+W^-)$
$76\,\text{GeV} < M(\ell^+\ell^-) < 106\,\text{GeV}$ $(2jZZ)$
$p_T(j) > 30$ GeV
$|\eta(j)| < 6.5$
$M(jj) > 60$ GeV
$M(j_f j_b) < 70$ GeV; $M(j_f j_b) > 100$ GeV
$|\Delta\eta(jj)| > 3.0$ $(2j2\ell2\nu)$
$|\Delta\eta(j_f j_b)| > 4.0$ $(2j4\ell, 4j\ell\nu, 4j\ell\ell)$
$|M(jjj) - M_{\text{top}}| > 15$ GeV $(4j\ell\nu, 4j\ell\ell)$
$|M(j\ell\nu_{rec}) - M_{\text{top}}| > 15$ GeV $(3\ell\nu + 2j, 4j\ell\nu)$
70 GeV $< M(j_c j_c) < 100$ GeV $(4j\ell\nu, 4j\ell\ell)$
$\Delta R(jj) > 0.3$ $(4j\ell\nu, 4j\ell\ell)$

Table 3. Basic cuts used at generation level.

- KM-LET and IAM E: these two scenarios contain no resonances at all. In the first case the Low Energy Theorem divergent contribution, neglecting all NLO terms, is unitarized using the KM method. In the second case the IAM procedure with $\alpha_4 = 0$ and $\alpha_5 = 0$ is employed. They will be compared to the no-Higgs scenario ($M_H \to \infty$ in the Unitary Gauge SM) where no unitarization is performed.

A detailed description of the comparison among all scenarios will be given for the channel $2jW^+W^- \to 2j\ell^+\ell^-\nu\bar\nu$, while for all other channels we will limit ourselves to the IAM A, IAM B, IAM D, KM-LET and no-Higgs cases only.

We have generated about half a million unweighted events for each channel and scenario and for the main backgrounds. All $\mathcal{O}(\alpha_{EM}^6)$ and $\mathcal{O}(\alpha_{EM}^4\alpha_S^2)$ processes have been included in our definition of the signal. At generation level the cuts of table 3 have been used. For each specific channel we have tried to determine which additional cuts could improve the separation between the unitarized model results and those obtained in the SM with a light Higgs . The specific cuts used at analysis level for each channel considered in the following are reported in appendix A. All results reported below are obtained after both basics and analysis cuts.
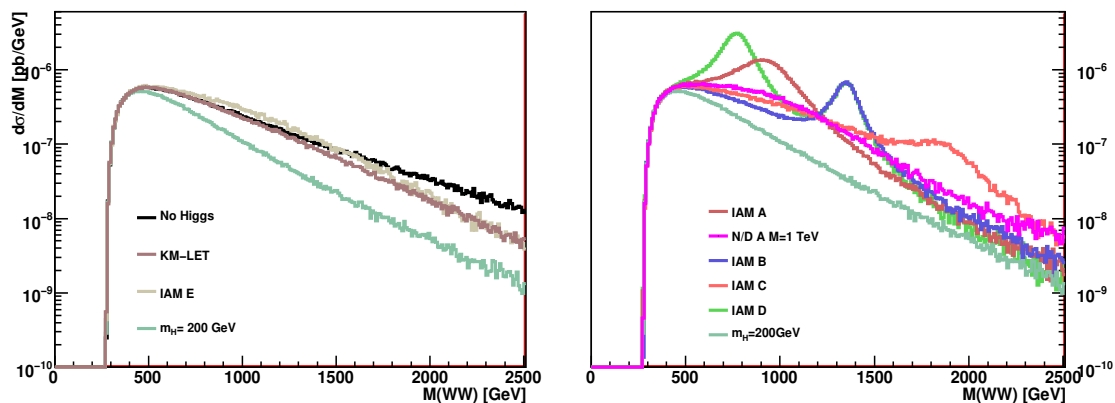
Figure 3. WW mass distributions in the $2jW^+W^- \to 2j\ell^+\ell^-\nu\bar{\nu}$ channel for different scenarios.

4.1 $2jW^+W^- \to 2j\ell^+\ell^-\nu\bar{\nu}$

The $2j\ell^+\ell^-\nu\bar{\nu}$ final state is one of the most important channels for the study of alternative symmetry breaking mechanisms at the LHC [38]. It is one of the channels in which the presence of two neutrinos in the final state does not allow the reconstruction of the invariant mass of the boson pair produced in association with two jets. This may appear as a limit since the invariant mass of the two bosons represents the center of mass energy in the case of the underlying boson boson scattering, and it is therefore the most appropriate variable to examine in order to discover signs of strong boson boson scattering. However, these final states are not affected by the huge QCD background which is typical of 4 jets plus two leptons final states. It has been shown [33, 37] that using invariant mass distribution of the two charged lepton can give very good results in discriminating between the light Higgs SM case and other scenarios.

As obvious, both $2jW^+W^- \to 2j\ell^+\ell^-\nu\bar{\nu}$ and $2jZZ \to 2j\ell^+\ell^-\nu\bar{\nu}$ contribute to this final state when the flavour of the two final state leptons are the same. However, cutting on the invariant $\ell^+\ell^-$ mass may easily discriminate between the two channels.

We start considering the case of $2jW^+W^- \to 2j\ell^+\ell^-\nu\bar{\nu}$ and we will use this channel to present a detailed analysis of the main features of the various unitarized models we consider.

In figure 3 one can see the invariant mass distributions of the WW pair in the different models.

These distributions cannot be measured in practice because the invariant mass of two leptons and two neutrinos cannot be reconstructed. It is however possible to compute them at MC level and we present them here in order to clearly see the behaviour of the various models.

On the left hand side of figure 3 the distributions for the three non resonant scenarios are reported and compared with the prediction of the SM with a light Higgs. Both unitarized distributions and the no-Higgs one are larger than the SM one and the difference between strongly and weakly coupled theories can be easily recognized. It is worth mentioning that the separation between the SM result and those for the no-Higgs, KM-LET
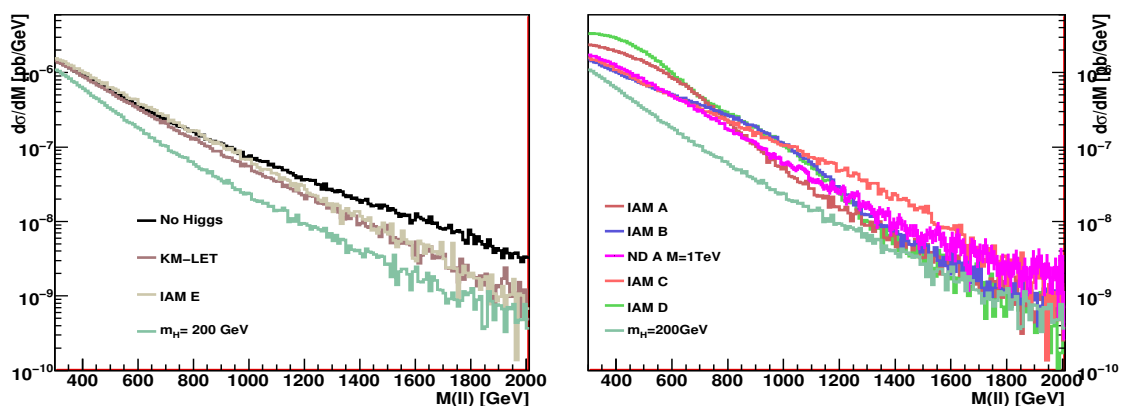
Figure 4. Lepton-lepton mass distributions in the $2jW^+W^- \to 2j\ell^+\ell^-\nu\bar{\nu}$ channel for different scenarios.

and IAM E cases is sharply increased by the additional cuts in appendix A which enhance the boson boson scattering contribution. The two unitarized models are very much similar, even if the unitarization scheme is different and in the IAM E case the NLO contributions are included. The no-Higgs scenario is practically indistinguishable from the previous ones up to an invariant mass of about 1.5 TeV. Above this threshold the effects of the violation of unitarity in the no-Higgs model manifest themselves. Because of this violation the no-Higgs model cannot be a consistent theory and can be valid only below an invariant mass of the order of a TeV. It has to be noticed however that at the LHC with design energy or lower, the vector vector pairs produced in the bulk of the events will have a mass smaller than 1.5 TeV and as a consequence the violation of unitarity will be of small practical relevance. Therefore the no-Higgs scenario can definitely be considered a good benchmark model to analyze the possibility of detecting new physics signals. This is also evident from the right hand side plot in figure 3, where one can recognise the peaking structure of the various unitarized models we have considered. If the distribution could be actually measured, the number of events of the various scenarios which develop resonances would be much larger than the ones of the left hand side. It is also evident from the right hand side plot of this figure that both scalar and vector resonances manifest themselves, as a consequence of the fact that the boson boson scattering subdiagrams in this case correspond both to $W^+W^- \to W^+W^-$ (which produce both a vector and a scalar resonance) and to $ZZ \to W^+W^-$ (which produce a scalar resonance).

In figure 4 the distributions of the invariant mass of the two charged leptons are presented. These distributions can be experimentally reconstructed and can be employed to discriminate among the different physical models. As it is obvious in these distributions all peaking structures have been smeared out but it is clear from the figures that the new physics models and the benchmark no-Higgs case can be clearly distinguished from a light Higgs scenario. The difference between the light Higgs case and new physics grows with the ll invariant mass for the non resonant models. On the other hand the number of events at

M_{cut}	no-H	KM	IAMA	IAMB	IAMC	IAMD	IAME	N/D	SM	$t\bar{t}jj$
300	.337	.303	.631	.400	.412	.867	.355	.367	.179	.173
400	.212	.186	.413	.274	.277	.547	.224	.240	.100	.0890
500	.139	.115	.246	.190	.187	.304	.142	.150	.0577	.0407
600	.0968	.0724	.132	.130	.126	.160	.0897	.0931	.0332	.0215
700	.0696	.0461	.0658	.0862	.0858	.0898	.0571	.0568	.0217	.0138

Table 4. Total cross section (in fb) for the $(W^+W^-)\ell^+\ell^-\nu\bar{\nu} + 2j$ channel with the full set of cuts in table 3 and table 18 in function of the minimum $\ell\ell$ invariant mass, $M(\ell\ell)$ (in GeV).
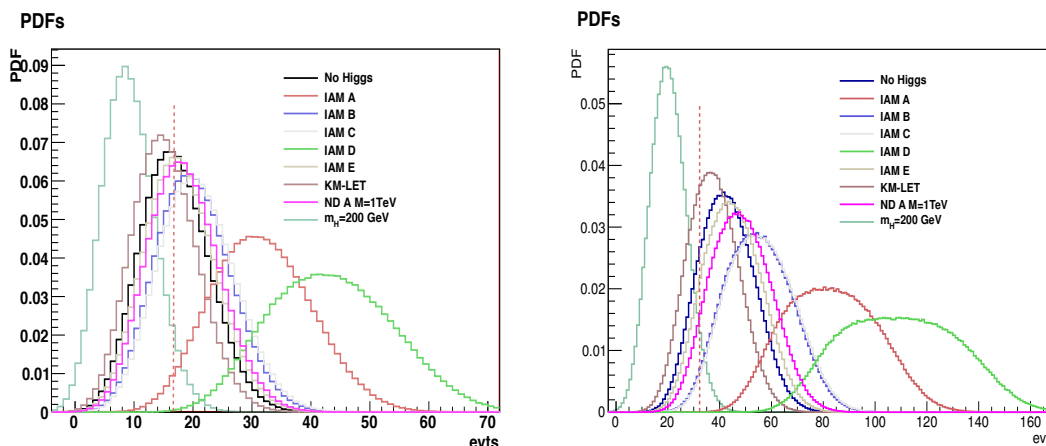
Figure 5. PDFs of the number of events in the $2jW^+W^- \to 2j\ell^+\ell^-\nu\bar{\nu}$ channel for $M_{\text{cut}} = 300\,\text{GeV}$, $L = 50\,\text{fb}^{-1}$ (left) and $M_{\text{cut}} = 400\,\text{GeV}$, $L = 200\,\text{fb}^{-1}$ (right).

high invariant mass decreases. One has to find a good compromise in selecting a range of masses which guarentees a good statistics and a sizeable difference between unitarization models and the SM.

This behaviour is exploited in table 4, where the cross sections are presented as a function of the minimun $M(ll)$ invariant mass. In the table the contribution of the $t\bar{t}jj$ background which can be misinterpreted for the signal when the $b's$ go undetected is also reported [38].

One can study the Probability Distribution Functions (PDFs) for the number of events which can be measured at a given luminosity. This exercise can be repeated for various M_{cut} in order to find the optimum cut for which the probability of dicriminating between the light Higgs case and new physics scenarios is largest. We show only the PDF's for the optimized cut. They are presented in figure 5 for two reference luminosities $L = 50\,\text{fb}^{-1}$ and $L = 200\,\text{fb}^{-1}$. Here and in the following, the PDF's are computed assuming Poissonian statistical fluctuations of the number of events computed by the MC and a theoretical error on the number of signal events which we model as a flat distribution of $\pm30\%$ from the actual value [37, 38].

$L(\,\mathrm{fb}^{-1})$	M_{cut}	no-H	KM	IAMA	IAMB	IAMC	IAMD	IAME	N/D
50	300	49.4%	37.8%	97.2%	68.5 %	71.6%	99.9%	55.4%	59.2 %
200	400	82.5%	68.4 %	100%	97.2 %	97.5%	100%	87.2%	91.8 %

Table 5. Probability to find a number of events larger than 95% limit of the SM (PBSM@95%CL) for the various scenarios in the $2jW^+W^- \to 2j\ell^+\ell^-\nu\bar{\nu}$ channel for two different luminosities $L = 50\,\mathrm{fb}^{-1}$ and $L = 200\,\mathrm{fb}^{-1}$. M_{cut} is expressed in GeV.

One can notice that the curves corresponding to models with no resonances (KM-LET, no-Higgs and IAM E) are closest to the light Higgs distribution and are not much different from each other. The ones which are most separated are the ones corresponding to models with resonances, the separation being larger for lower mass resonances. In the plots the vertical line represents the 95% limit of the light Higgs distribution. We therefore compute what we call the PBSM@95%CL (Probability Beyond the SM at 95% Confidence Level) for the various scenarios as the probability that a number of events larger than the 95% limit occurs. The results, reported in table 5, show quantitatively that the probability of excluding the no-Higgs model lies among the other non resonant ones. Models with low mass resonances can be easily excluded or verified already with luminosity $L = 50\,\mathrm{fb}^{-1}$. On the contrary a higher luminosity is required for models which are non resonant or contain high mass resonances.

4.2 The other two neutrinos final states

The final state with two jets, two neutrinos and two charged leptons of different sign can result from WW or ZZ production and decay. In a complete six fermion approach, when the two leptons are of the same flavour, the separation of the two channels has to rely on cuts on the l^+l^- mass. Another well known and interesting channel for studying boson boson scattering is $2j\ell^\pm\ell^\pm\nu\nu$ in which the two leptons are of the same sign. These two channels will be discussed in the following in the context of unitarized models.

4.2.1 The $2jZZ \to 2j\ell^+\ell^-\nu\bar{\nu}$ channel

As already mentioned, this channel has been separated from the $2jWW \to 2j\ell^+\ell^-\nu\bar{\nu}$ with same flavour leptons requiring $|M(\ell\ell) - M_Z| < 15\,\mathrm{GeV}$. A ZZ final state can be produced in two different scattering processes: $ZZ \to ZZ$ and $W^+W^- \to ZZ$. As a consequence this final state has many analogies with the channel we have previously examined. For such a reason we do not present here the final state (not measurable) ZZ invariant mass distribution. Instead we consider the transverse ZZ mass:

$$M_T^2(ZZ) = [\sqrt{M_Z^2 + p_T^2(\ell\ell)} + \sqrt{M_Z^2 + p_{\mathrm{Tmiss}}^2}]^2 - |\vec{p_T}(\ell\ell) + \vec{p}_{\mathrm{Tmiss}}|^2. \qquad (4.1)$$

The transverse mass distributions for the IAM A, IAM B, IAM D and KM-LET models after basic and analysis cuts are reported in figure 6 and compared with the no-Higgs and the light Higgs SM scenarios. It is rather evident that with the full set of cuts the non SM scenarios differ significantly from the light Higgs case. It is in particular interesting
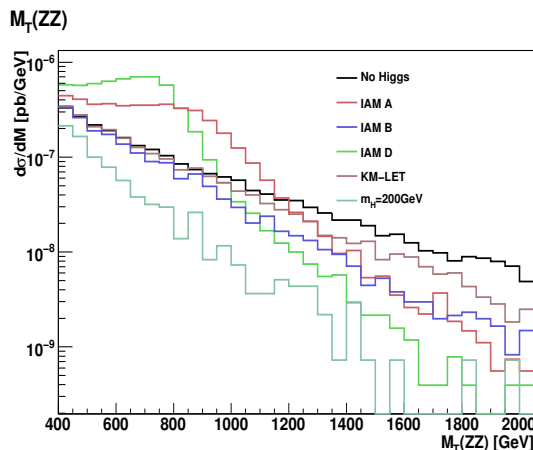
Figure 6. Transverse mass distributions of the ZZ-system in the $2jZZ \to 2j\ell^+\ell^-\nu\bar{\nu}$ channel with full set of cuts, table 3 and table 18 of appendix A.
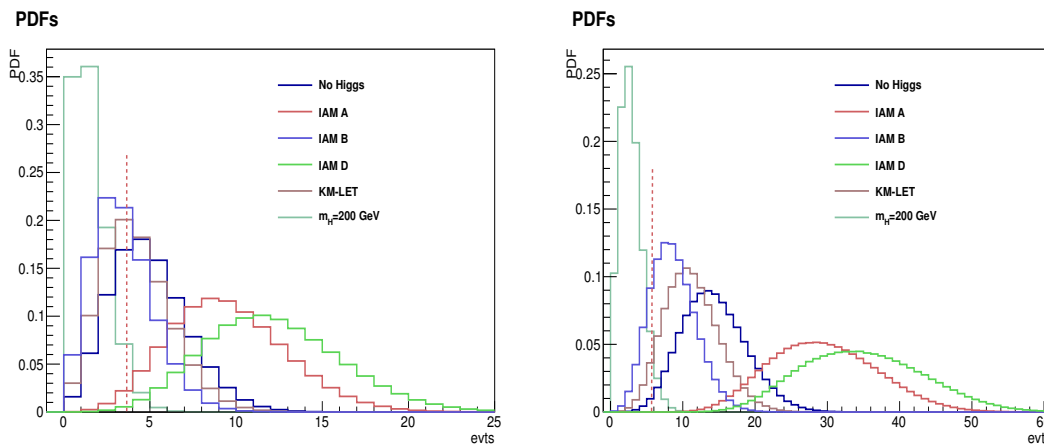
M_{cut}	no-Higgs	KM-LET	IAM A	IAM B	IAM D	SM
300	.143	.125	.249	.109	.319	.0540
400	.120	.105	.224	.0886	.291	.0396
500	.0887	.0739	.181	.0589	.233	.0214
600	.0691	.0537	.145	.0408	.172	.0118
700	.0547	.0395	.110	.0285	.103	.00697

Table 6. Total cross section (in fb) for the $(ZZ)\ell^+\ell^-\nu\bar{\nu} + 2j$ channel with the full set of cuts in table 3 and table 18 in function of the minimum $M_T(ZZ)$ (in GeV).

that in this channel the IAM A and IAM D scenarios are the two models which differ the most from the SM predictions. They both present a relatively light scalar resonance. On the contrary for the IAM B model the signal is not so prominent since its vector resonance cannot appear in this channel.

Even if the transverse mass does not directly correspond to vector vector scattering center of mass energy, the KM-LET and no-Higgs models have, as before, a similar behaviour for low invariant masses while they start to deviate from each other above 1 TeV. In terms of cross sections their difference is only of the order of 10% if we do not restrict ourselves to very high invariant mass cuts. The results for the cross sections are reported in table 6 . The expected number of events is rather small.

From the values reported in the table 6, we have determined the cut which maximizes the separation of the different scenarios which turns out to be $M_{\mathrm{cut}} = 500\,\mathrm{GeV}$ for $L = 50\,\mathrm{fb}^{-1}$ and $M_{\mathrm{cut}} = 600\,\mathrm{GeV}$ for $L = 200\,\mathrm{fb}^{-1}$. The corresponding Probability Distribution Functions are shown in figure 7 and confirm that for the IAM A and IAM D models we are nearly certain to be able to observe a deviation from the SM already with $50\,\mathrm{fb}^{-1}$. For all considered models, with $200\,\mathrm{fb}^{-1}$ of data, the probability of observing a discrepancy between the experimental results is above 80%.

Figure 7. PDFs of the number of events in the $(ZZ)\ell^+\ell^-\nu\bar{\nu} + 2j$ channel for $M_{\text{cut}} = 500\,\text{GeV}$, $L = 50\,\text{fb}^{-1}$ (left) and $M_{\text{cut}} = 600\,\text{GeV}$, $L = 200\,\text{fb}^{-1}$ (right).

$L(\text{fb}^{-1})$	M_{cut} (GeV)	no-Higgs	KM-LET	IAM A	IAM B	IAM D
50	500	68.8428%	56.5684%	97.3776%	41.4185%	99.4127%
200	600	98.5618%	93.7842%	99.9998%	80.8113%	100%

Table 7. PBSM@95%CL, defined in subsection 4.1, for the various scenarios in the $2jZZ \rightarrow 2j\ell^+\ell^-\nu\bar{\nu}$ channel.

If one compares table 7 with table 5, it is apparent that in order to discover signals of new physics in boson boson scattering processes, one must examine all possible channels because some models can produce a modest signal in some channels while being easily detectable in others.
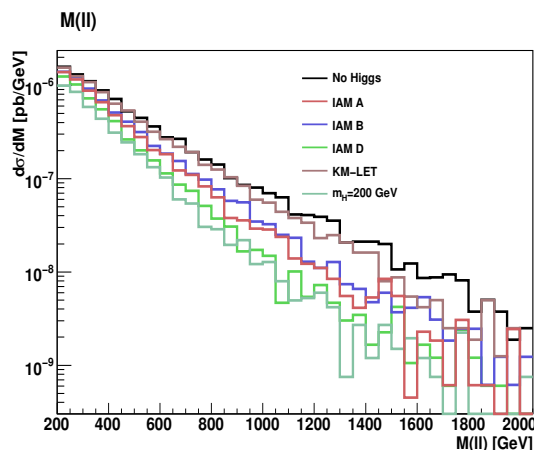
4.2.2 The $2j\ell^\pm\ell^\pm\nu\nu$ channel

The channel with two neutrinos and two same sign leptons in the final state has long been considered one of the most promising because of the absence of large backgrounds. We will however see that the relevance of this channel depends quite a bit on which theory we are examining, as this final state corresponds to an underlying scattering of two same sign W's.

As usual we start considering the invariant mass distributions of the two leptons. They are shown in figure 8. The full set of cuts has been imposed. No peaking structure is present. This reflects the fact that, for the models we have examined, neither scalar nor vector resonances can be produced in this channel. In this case the no-Higgs and KM-LET models, which do not develop resonances in any channel, give the largest predictions. The lowest curve is as usual the SM light Higgs scenario. All the others fall in between.

These results are made quantitative by the values of the cross sections as a function of the dilepton invariant mass cut which is shown in table 8 and by the PDF distributions of figure 9.

One sees immediately that the number of events produced in this channel is not large. Moreover the IAM A, IAM B and IAM D models can hardly be distinguished from the

Figure 8. Distributions of the $\ell\ell$ invariant mass for the $2j\ell^{\pm}\ell^{\pm}\nu\nu$ channel with full set of cuts, table 3 and table 18.

M_{cut}	no-Higgs	KM-LET	IAM A	IAM B	IAM D	SM
200	.435	.407	.310	.332	.254	.206
300	.290	.267	.183	.201	.141	.114
400	.191	.171	.107	.120	.0768	.0629
500	.129	.112	.0643	.0744	.0430	.0351
600	.0886	.0760	.0403	.0474	.0250	.0194
700	.0614	.0517	.0250	.0304	.0150	.0112

Table 8. Total cross section (in fb) for the $\ell^{\pm}\ell^{\pm}\nu\nu + 2j$ channel with the full set of cuts in table 3 and table 18 in function of the minimum $\ell\ell$ invariant mass, $M(ll)$ (in GeV).
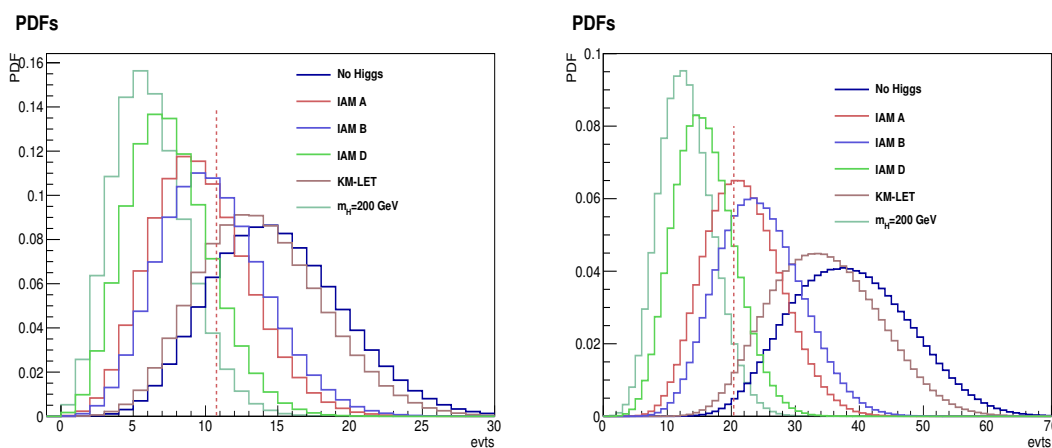
Figure 9. PDFs of the number of events in the $\ell^{\pm}\ell^{\pm}\nu\nu + 2j$ channel for $M_{\text{cut}} = 300\,\text{GeV}$, $L = 50\,\text{fb}^{-1}$ and $M_{\text{cut}} = 400\,\text{GeV}$, $L = 200\,\text{fb}^{-1}$.

$L(\text{fb}^{-1})$	M_{cut} (GeV)	no-Higgs	KM-LET	IAM A	IAM B	IAM D
50	300	81.42%	74.36%	34.48%	44.36%	13.60%
200	400	98.96%	96.92%	57.72%	72.03%	17.21%

Table 9. PBSM@95%CL, defined in subsection 4.1, for the $\ell^{\pm}\ell^{\pm}\nu\nu + 2j$ channel.

light Higgs SM case. Table 9 shows however that non resonant unitarized models can give detectable signals of new physics at high luminosity.

In conclusion, one has to be very careful in relying on this channel for detecting new physics because, even if it has the advantage of very small backgrounds, it is not sensitive to the types of resonances considered here. On the other hand it achieves one of the best dicriminating powers for scenarios without resonances.

4.3 Final states in which the boson boson mass can be reconstructed

The final states in which the boson boson mass M_{VV} can be reconstructed are those in which at most one neutrino is produced, namely $\ell\nu + 4j$, $\ell^{+}\ell^{-} + 4j$, $3\ell\nu + 2j$ and $4\ell + 2j$. Reconstructing M_{VV} is very useful because it corresponds to C.M. energy of the underlying boson boson scattering. As it happens for on-shell boson boson scattering, the differences between weakly and strongly interacting theories manifest themselves more clearly at high invariant mass.

The $4\ell + 2j$ channel, with two opposite sign charged lepton pairs has a very low cross section and it corresponds to a ZZ final state.

In order to compute the invariant mass of the two bosons, when a neutrino is present in the final state its longitudinal momentum is reconstructed with the usual procedure of forcing the invariant mass of the $\ell\nu$ pair to be equal to the W boson nominal mass,

$$(p^{\ell} + p^{\nu})^2 = M_W^2. \tag{4.2}$$

This determines, up to a two fold ambiguity, the longitudinal component of the neutrino momentum [36].

The $4j\ell\nu$ and $\ell^{+}\ell^{-} + 4j$ channels contain 4 final state jets. Two of them, the most forward and most backward one, will provide tagging and will be required to be well separated and energetic. The two central ones will be considered as candidates to reconstruct an electroweak boson. The boson boson invariant mass will be assumed to be that of the system formed by the two central jets, the charged lepton and the reconstructed neutrino.

The cross section of the four jet channels is relatively large, however they are affected by substantial backgrounds. In particular $V + 4j$ QCD processes give very large rates even after cut optimization. For the $4j\ell\nu$ final state also $t\bar{t}$ and $t\bar{t} + jets$ production has to be considered carefully. We have discussed in detail in our previous papers [36–38] how to deal with these backgrounds. Here we only recall that when computing the Probablity Distribution Functions we will attribute a statistical error to these contributions but no theoretical error since we assume that they can be measured in nearby regions and extrapolated to the kinematic range of interest for VV scattering.
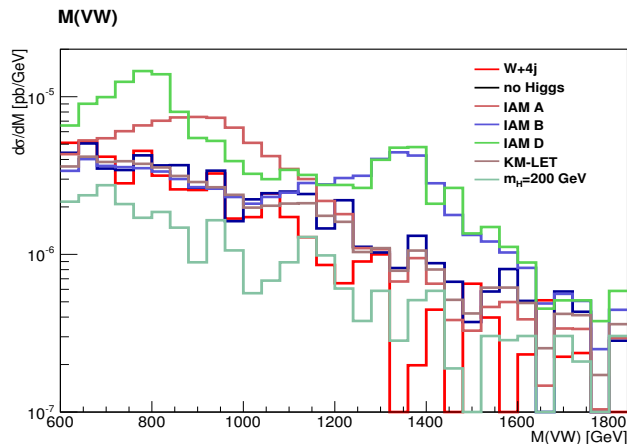
Figure 10. Distributions of the mass of the VW-system for the $\ell^\pm \nu + 4j$ channel with full set of cuts, table 3 and table 18.

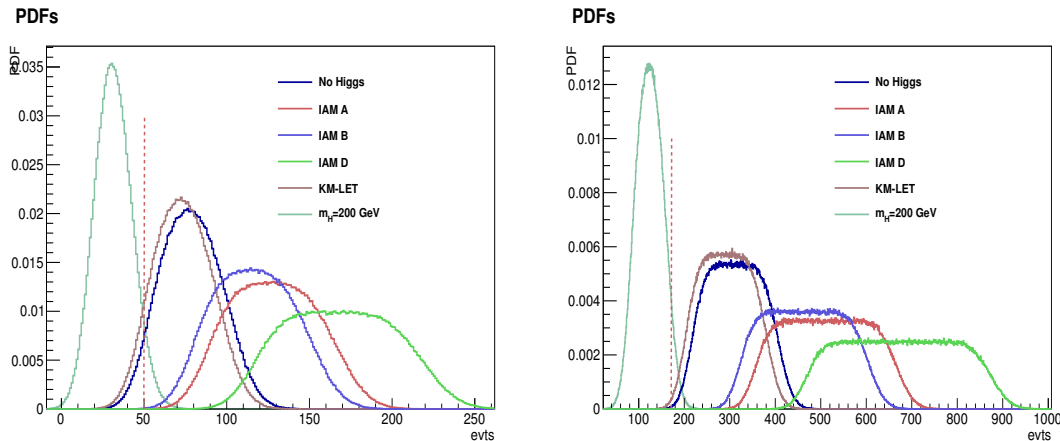| M_{cut}	no-Higgs	KM-LET	IAM A	IAM B	IAM D	SM	$W + 4j$	$t\bar{t} + 2j$
600	2.36	2.23	3.66	3.04	5.46	1.048	2.03	.432
800	1.558	1.46	2.56	2.32	3.36	.618	1.15	.167
1000	.966	.877	1.13	1.76	1.90	.338	0.62	.0617
1200	.526	.478	.414	1.26	1.27	.188	0.30	.0264

Table 10. Total cross section (in fb) for the $\ell^\pm \nu + 4j$ channel with the full set of cuts in table 3 and table 18 in function of the minimum $j_c j_c \ell \nu$ invariant mass (in GeV).

4.3.1 The $4j\ell\nu$ channel

The final state of this cannel corresponds to both ZW and WW production. The invariant mass distributions of the boson pair with the full set of cuts is reported in figure 10. The corresponding cross sections for various values of the invariant mass cut are given in table 10. Both scalar and vector resonances are clearly visible in this channel. The $W + 4j$ background is much larger than the SM electroweak prediction; it turns out to be of the same order as the expected yield of the KM-LET and no-Higgs non resonant models. It must be pointed out that this background, computed at tree level with MADEVENT at a fixed scale, has been rescaled to the scale $Q = \hat{H}'_T/2$, $\hat{H}'_T = \sum_i^4 p_T(j) + E_T(W)$, where $E_T^2(W) = p_T^2(W) + M^2(W)$ [44]. With this dynamical scale the $W + 4j$ contribution has sensibly decreased compared to the fixed scale results.

Examining the PDF distributions of figure 11, one realizes that the situation is similar to the one already discussed for the $2jW^+W^- \rightarrow 2j\ell^+\ell^-\nu\bar{\nu}$ channel: the models with the lightest resonances are the ones which can be most easily distinguished from the Standard Model with a light Higgs. The KM-LET has the smallest cross section of all unitarized models. It is however well separated by the SM case especially with a luminosity of $200\,\text{fb}^{-1}$. The no-Higgs model behaves similarly to the KM-LET one, confirming that, even if unphysical, this model has good properties as a benchmark case.

Figure 11. PDFs of the number of events in the $\ell^{\pm}\nu + 4j$ channel for $M_{\mathrm{cut}} = 800\,\mathrm{GeV}$, $L = 50\,\mathrm{fb}^{-1}$ (left) and $M_{\mathrm{cut}} = 800\,\mathrm{GeV}$, $L = 200\,\mathrm{fb}^{-1}$ (right).

$L(\mathrm{fb}^{-1})$	M_{cut} (GeV)	no-Higgs	KM-LET	IAM A	IAM B	IAM D
50	800	94.51%	91.03%	99.99%	99.97%	100%
200	800	99.93%	99.64%	100%	100%	100%

Table 11. PBSM@95%CL, defined in subsection 4.1, for the $\ell^{\pm}\nu + 4j$ channel.

Finally, the number of events is rather large already at $L = 50\,\mathrm{fb}^{-1}$ and the discriminating power described by the PBSM@95%CL values of table 11 is rather encouraging.

4.3.2 The $\ell^{+}\ell^{-} + 4j$ channel

This channel is in many respects similar to the one we have just considered. The final state in this case corresponds to ZW or ZZ production in the boson boson scattering processes. There are no contributions from $t\bar{t} + 2j$ but the $Z + 4j$ background is large. It has been evaluated with the running scale $Q = \hat{H}'_T/2$ as before.

In figure 12 we show the distribution of the invariant mass of the two final state bosons for the different models. After all cuts, the signal cross sections in this channel are about five times smaller than those of the $4j\ell\nu$ channel, as shown in table 12. This implies that the discriminating power for new physics models is sensibly lower, as can be seen from figure 13 and table 13.

The pattern of the distributions in figure 13 is analogous to the one in the $4j\ell\nu$ channel: models with light resonances are easily distinguished from the SM and models without resonant states give smaller predictions which are in rough agreement among themselves. With $L = 200\,\mathrm{fb}^{-1}$ all models have a high probability of producing a number of events larger than the 95%CL for the SM. The KM-LET model, which is the one least likely to be detected sports a PBSM@95%CL of 93%. At $L = 50\,\mathrm{fb}^{-1}$ the PBSM@95%CL for the KM-LET case drops to about 60%.

M(VZ)
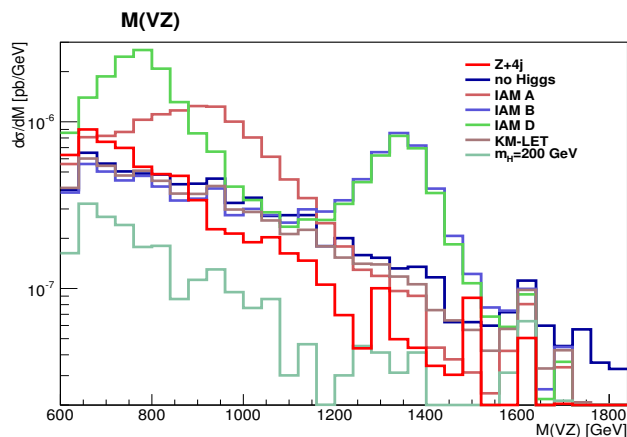
Figure 12. Distributions of the mass of the VZ-system for the $\ell^+\ell^- + 4j$ channel with full set of cuts, table 3 and table 18.

M_{cut}	no-Higgs	KM-LET	IAM A	IAM B	IAM D	SM	$Z + 4j$
600	.308	.274	.532	.388	.795	.0969	.269
800	.204	.173	.369	.294	.424	.0500	.128
1000	.120	.0975	.138	.223	.211	.0258	.059
1200	.0657	.0511	.0396	.167	.156	.0154	.027

Table 12. Total cross section (in fb) for the $\ell^+\ell^- + 4j$ channel with the full set of cuts in table 3 and table 18 in function of the minimum $j_c j_c \ell\ell$ invariant mass (in GeV).
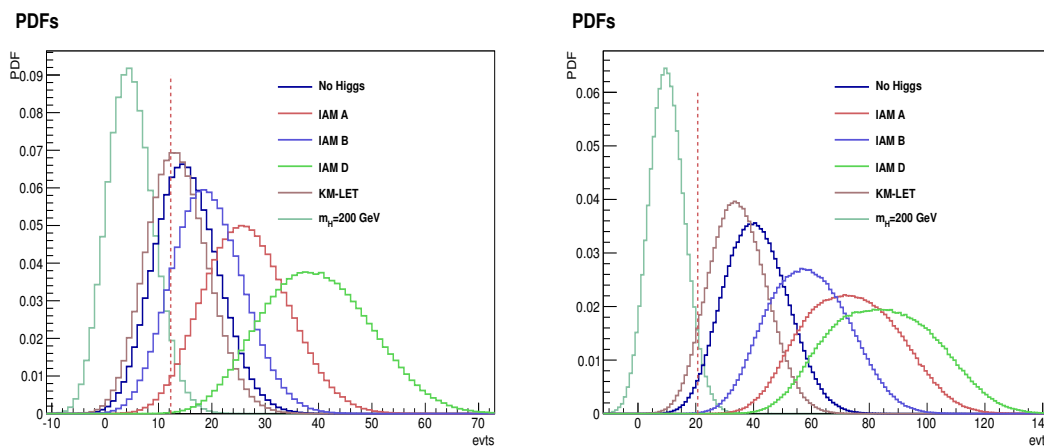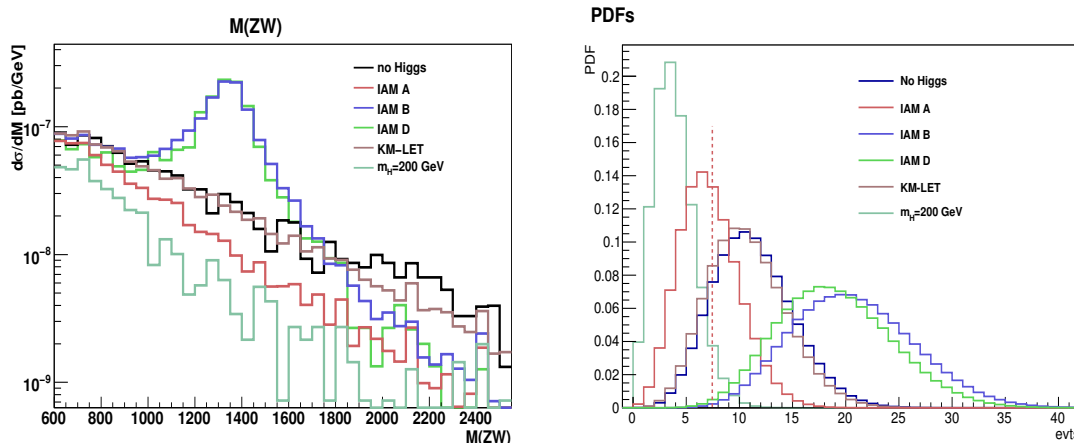

Figure 13. PDFs of the number of events in the $\ell^+\ell^- + 4j$ channel for $M_{\mathrm{cut}} = 600\,\mathrm{GeV}$, $L = 50\,\mathrm{fb}^{-1}$ (left) and $M_{\mathrm{cut}} = 800\,\mathrm{GeV}$, $L = 200\,\mathrm{fb}^{-1}$ (right).

4.3.3 The $3\ell\nu + 2j$ channel

This final state does not suffer from the huge backgrounds stemming from $t\bar{t}$ or $V + 4j$ production. The final state corresponds to ZW production in the underlying scattering

$L(\text{fb}^{-1})$	M_{cut} (GeV)	no-Higgs	KM-LET	IAM A	IAM B	IAM D
50	600	68.36%	57.90%	97.43%	85.61%	99.95%
200	800	97.70%	92.81%	99.99%	99.97 .%	100%

Table 13. PBSM@95%CL, defined in subsection 4.1, for the $\ell^+\ell^- + 4j$ channel for $L = 50\,\text{fb}^{-1}$ and $L = 200\,\text{fb}^{-1}$.

Figure 14. Distributions of the mass of the WZ-system for the $3\ell\nu + 2j$ channel with full set of cuts, table 3 and table 18 (left). PDFs of the number of events for $M_{\text{cut}} = 600\,\text{GeV}$ and $L = 200\,\text{fb}^{-1}$ (right).

process. Hence scalar resonances cannot be formed. This is clearly visible in figure 14 where we show on the left the boson boson invariant mass distribution and on the right the PDF for $L = 200\,\text{fb}^{-1}$ and $M_{\text{cut}} = 600\,\text{GeV}$. One notices immediately, comparing with the results obtained for the two previous channels, that the PDF for the IAM A model, which develops a scalar resonance, is now closer to the SM predictions than the KM-LET model.

The total cross sections as a function of the boson boson invariant mass lower cut are given in table 14. The reported values are now in attobarns and this is reflected in a small expected number of events at the LHC. The PBSM@95%CL are shown in table 15. With $50\,\text{fb}^{-1}$ of data only the IAM B and IAM D models have a reasonable chance of manifesting themselves in sizable deviations from the SM. At $L = 200\,\text{fb}^{-1}$ these two models would be almost certainly revealed while the PBSM@95%CL for both the no-Higgs and the KM-LET models are above 80%.
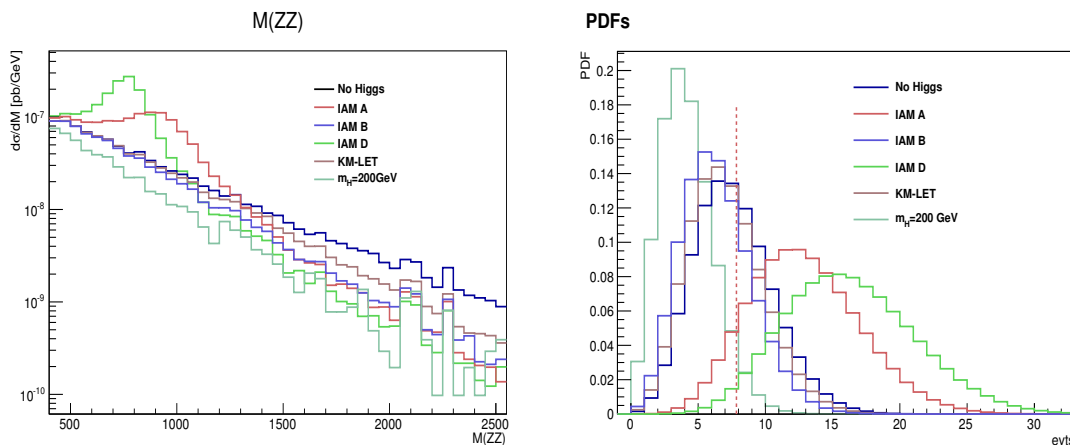
4.3.4 The $4\ell + 2j$ channel

The present channel has some similarities with the $3\ell\nu + 2j$ channel above. In some sense it is complementary to it. In fact it corresponds to the formation of a ZZ pair and this implies that no vector resonance can be formed in this channel. In figure 15 the ZZ invariant mass distribution is shown on the left while the PDF for $L = 200\,\text{fb}^{-1}$ and $M_{\text{cut}} = 500\,\text{GeV}$ are on the right. Figure 15 clearly shows that the models which produce scalar resonances are well separated from the SM. On the contrary, the IAM B model, in which only a vector res-

M_{cut}	no-Higgs	KM-LET	IAM A	IAM B	IAM D	SM
600	53.8	51.2	33.5	101.	92.6	17.0
800	37.6	34.3	19.2	84.6	78.8	8.92
1000	25.6	22.5	11.0	72.0	68.7	4.42
1200	17.3	14.7	6.21	57.1	56.1	2.38

Table 14. Total cross section (in ab) for the $3\ell\nu + 2j$ channel with the full set of cuts in table 3 and table 18 in function of the minimum $3\ell\nu$ invariant mass (in GeV).

$L(\text{fb}^{-1})$	M_{cut} (GeV)	no-Higgs	KM-LET	IAM A	IAM B	IAM D
50	600	46.30%	43.27%	21.51%	83.71%	79.51%
200	600	84.12%	80.81%	43.47%	99.73%	99.38%

Table 15. PBSM@95%CL, defined in subsection 4.1, for the $3\ell\nu + 2j$ channel.

Figure 15. Distributions of the mass of the ZZ-system for the $4\ell + 2j$ channel with full set of cuts, table 3 and table 18 (left). PDFs for $M_{\text{cut}} = 500\,\text{GeV}$ and $L = 200\,\text{fb}^{-1}$ (right).

onance is present, appears even more difficult to disentangle from the light-Higgs scenario than the non resonant ones.

In table 16 the values of the cross sections in attobarns are reported. These very modest cross sections imply that no stringent cut can be imposed and as a consequence the discriminatory power of this channel is smaller than that of all other final states presented in this paper, as can be seen from table 17. Only at $L = 200\,\text{fb}^{-1}$ this channel could be useful for the IAM A and IAM D models.

5 Conclusions

We have described in some detail how Unitarized Models have been implemented in the PHANTOM MonteCarlo. We have then compared the predictions of this new implementation

M_{cut}	no-Higgs	KM-LET	IAM A	IAM B	IAM D	SM
400	44.7	41.9	72.0	38.5	89.6	25.5
500	35.6	32.8	62.0	29.5	79.0	18.4
600	28.2	25.4	52.9	22.2	67.8	13.5
700	22.2	19.4	44.0	16.4	52.0	9.64
800	17.8	14.9	34.6	12.2	26.0	7.09
900	14.0	11.4	23.6	8.97	10.9	5.19

Table 16. Total cross section in ab for the $4\ell + 2j$ channel with the full set of cuts in table 3 and table 18 in function of the minimum 4ℓ invariant mass (in GeV).

$L(\text{fb}^{-1})$	M_{cut} (GeV)	no-Higgs	KM-LET	IAM A	IAM B	IAM D
200	500	43.86%	36.31%	89.60%	27.41%	97.36%

Table 17. PBSM@95%CL, defined in subsection 4.1, for the $4\ell + 2j$ channel.

which makes use of full six fermion final state matrix elements calculations with those obtained with old EVBA methods and presented in the literature. The agreement between the two calculations depends rather strongly on the separation between the two tag jet, a variable which cannot be controlled in EVBA. The shape of the distribution of the invariant mass of the two vector boson system is in any case quite different, in particular for smaller invariant masses.

Using the new tool we have adressed the important issue of the possibility of uncovering new physics signals in vector boson scattering processes at LHC. For this we have considered some typical examples of unitarized models. These can be divided in two sets: those which predict the formation of resonances, which in the cases we have examined can be scalar or vector in nature, and those in which no resonant state is formed.

Our analysis has concentrated on counting experiments which look for an excess of boson boson scattering events compared with SM expectations in the large invariant mass region. Our results show that these experiments can detect new physics at 14 TeV for all considered scenarios using a luminosity of 200 fb^{-1}. At 50 fb^{-1} instead the results depend on the particular channel and scenario under consideration. Since models with no resonance, models with scalar resonances and models with vector resonances behave differently in different final states we stress the importance of carefully analyzing all possible channels and not only the ones with largest cross section or smallest background.

Acknowledgments

A Selection cuts

Processes / Cuts	$2j\ell^+\ell'^-\nu\bar\nu$ (W^+W^-)	$2j\ell^+\ell^-\nu\bar\nu$ (ZZ)	$2j\ell^\pm\nu\ell^\pm\nu$	$4j\ell\nu$	$4j\ell\ell$	$2j3\ell\nu$	$2j4\ell\nu$
$|\eta(\ell^\pm)| <$	2.0			2.0		2.0	
$M(j_f j_b) >$	1000	800		1000	1000	1000	800
$|\Delta\eta(j_f j_b)| >$	4.8	4.5	4.5	4.8	4.8	4.8	
$p_T(j_c) >$				70	60		
$p_T(j_c j_c) >$					200		
$p_T(\ell\nu) >$				200		200	
$p_{\mathrm{Tmiss}} >$		120		100			
$p_T(\ell^+\ell^-) >$		120			200	200	100
$p_T(\ell) >$			50				
$2minp_T(j) <$			120				
$E(j) >$	180						
$max|\eta(j)| >$	2.5		2.5		2.8		
$|\eta(j)| >$	1.3	1.9				1.2	
$|\Delta\eta(Vj)| >$				0.6	1.1	1.5	
$\Delta\eta(\ell j) >$	0.8	1.3					
$\Delta R(\ell j) >$	1		1.5				
$\Delta R(Zj) >$							1
$M(\ell j) >$	180						
$M(Vj) >$					300		
$|\vec{p}_T(\ell_1) - \vec{p}_T(\ell_2)| >$	220		150				
$|\vec{p}_T(\ell^+\ell^-) - \vec{p}_T^{miss}| >$		290					
$\cos(\delta\phi_{\ell\ell}) <$	-0.6		-0.6				
$\cos(\delta\phi_{ZZ}) <$							-0.4
$\Delta R(\ell^+\ell^-) <$					1.0		

Table 18. Additional selection cuts for the various channels. All masses, momenta and energies are expressed in GeV.

References

[1] ATLAS collaboration, G. Aad et al., *Combined search for the Standard Model Higgs boson using up to 4.9 fb^{-1} of pp collision data at $\sqrt{s} = 7$ TeV with the ATLAS detector at the LHC*, arXiv:1202.1408 [INSPIRE].

[2] CMS collaboration, S. Chatrchyan et al., *Combined results of searches for the Standard Model Higgs boson in pp collisions at $\sqrt{s} = 7$ TeV*, arXiv:1202.1488 [INSPIRE].

[3] M. Veltman, *Second threshold in weak interactions*, Acta Phys. Polon. **B 8** (1977) 475 [INSPIRE].

[4] M. Veltman, *Large Higgs mass and μ-e universality*, Phys. Lett. **B 70** (1977) 253 [INSPIRE].

[5] B.W. Lee, C. Quigg and H. Thacker, *The strength of weak interactions at very high-energies and the Higgs boson mass*, Phys. Rev. Lett. **38** (1977) 883 [INSPIRE].

[6] B.W. Lee, C. Quigg and H. Thacker, *Weak interactions at very high-energies: the role of the Higgs boson mass*, Phys. Rev. **D 16** (1977) 1519 [INSPIRE].

[7] G. Passarino, *Large masses, unitarity and one loop corrections*, Phys. Lett. **B 156** (1985) 231 [INSPIRE].

[8] G. Passarino, *WW scattering and perturbative unitarity*, Nucl. Phys. **B 343** (1990) 31 [INSPIRE].

[9] A. Djouadi, *The anatomy of electro-weak symmetry breaking. I: the Higgs boson in the Standard Model*, Phys. Rept. **457** (2008) 1 [hep-ph/0503172] [INSPIRE].

[10] ATLAS collaboration, G. Aad et al., *Expected performance of the ATLAS experiment — detector, trigger and physics*, arXiv:0901.0512 [INSPIRE].

[11] CMS collaboration, G. Bayatian et al., *CMS technical design report, volume II: physics performance*, J. Phys. **G 34** (2007) 995 [INSPIRE].

[12] M.S. Chanowitz, *Strong WW scattering at the end of the 90's: theory and experimental prospects*, hep-ph/9812215 [INSPIRE].

[13] T. Appelquist and C.W. Bernard, *Strongly interacting Higgs bosons*, Phys. Rev. **D 22** (1980) 200 [INSPIRE].

[14] A.C. Longhitano, *Heavy Higgs bosons in the Weinberg-Salam model*, Phys. Rev. **D 22** (1980) 1166 [INSPIRE].

[15] A.C. Longhitano, *Low-energy impact of a heavy Higgs boson sector*, Nucl. Phys. **B 188** (1981) 118 [INSPIRE].

[16] T. Appelquist and G.-H. Wu, *The electroweak chiral Lagrangian and new precision measurements*, Phys. Rev. **D 48** (1993) 3235 [hep-ph/9304240] [INSPIRE].

[17] R. Contino, T. Kramer, M. Son and R. Sundrum, *Warped/composite phenomenology simplified*, JHEP **05** (2007) 074 [hep-ph/0612180] [INSPIRE].

[18] G. Giudice, C. Grojean, A. Pomarol and R. Rattazzi, *The strongly-interacting light Higgs*, JHEP **06** (2007) 045 [hep-ph/0703164] [INSPIRE].

[19] R. Barbieri, B. Bellazzini, V.S. Rychkov and A. Varagnolo, *The Higgs boson from an extended symmetry*, Phys. Rev. **D 76** (2007) 115008 [arXiv:0706.0432] [INSPIRE].

[20] M.J. Duncan, G.L. Kane and W. Repko, *WW physics at future colliders*, Nucl. Phys. **B 272** (1986) 517 [INSPIRE].

[21] D. Dicus and R. Vega, *WW production from pp collisions*, *Phys. Rev. Lett.* **57** (1986) 1110 [INSPIRE].

[22] R.N. Cahn, S.D. Ellis, R. Kleiss and W. Stirling, *Transverse momentum signatures for heavy Higgs bosons*, *Phys. Rev.* **D 35** (1987) 1626 [INSPIRE].

[23] V.D. Barger, T. Han and R. Phillips, *Improved transverse mass variable for detecting Higgs boson decays into Z pairs*, *Phys. Rev.* **D 36** (1987) 295 [INSPIRE].

[24] R. Kleiss and W. Stirling, *Tagging the Higgs*, *Phys. Lett.* **B 200** (1988) 193 [INSPIRE].

[25] V.D. Barger, T. Han and R. Phillips, *Improving the heavy Higgs boson two-charged-lepton-two-neutrino signal*, *Phys. Rev.* **D 37** (1988) 2005 [INSPIRE].

[26] V.D. Barger, K.-M. Cheung, T. Han and R. Phillips, *Strong W^+W^+ scattering signals at pp supercolliders*, *Phys. Rev.* **D 42** (1990) 3052 [INSPIRE].

[27] U. Baur and E. Glover, *Tagging the Higgs boson in $pp \to W^+W^- jj$*, *Phys. Lett.* **B 252** (1990) 683 [INSPIRE].

[28] D. Dicus, J. Gunion and R. Vega, *Isolating the scattering of longitudinal W^+'s at the SSC using like sign dileptons*, *Phys. Lett.* **B 258** (1991) 475 [INSPIRE].

[29] V.D. Barger, K.-M. Cheung, T. Han and D. Zeppenfeld, *Single forward jet tagging and central jet vetoing to identify the leptonic WW decay mode of a heavy Higgs boson*, *Phys. Rev.* **D 44** (1991) 2701 [*Erratum ibid.* **D 48** (1993) 5444] [INSPIRE].

[30] D. Dicus, J. Gunion, L. Orr and R. Vega, *Isolating purely leptonic signals for strong W scattering using antitagging jet tagging and lepton isolation*, *Nucl. Phys.* **B 377** (1992) 31 [INSPIRE].

[31] J. Bagger et al., *The strongly interacting WW system: gold plated modes*, *Phys. Rev.* **D 49** (1994) 1246 [hep-ph/9306256] [INSPIRE].

[32] V.D. Barger, R. Phillips and D. Zeppenfeld, *Mini-jet veto: a tool for the heavy Higgs search at the LHC*, *Phys. Lett.* **B 346** (1995) 106 [hep-ph/9412276] [INSPIRE].

[33] J. Bagger et al., *CERN LHC analysis of the strongly interacting WW system: gold plated modes*, *Phys. Rev.* **D 52** (1995) 3878 [hep-ph/9504426] [INSPIRE].

[34] D.L. Rainwater and D. Zeppenfeld, *Observing $H \to W^{(*)}W^{(*)} \to e^{\pm}\mu^{\mp}\not{p}_T$ in weak boson fusion with dual forward jet tagging at the CERN LHC*, *Phys. Rev.* **D 60** (1999) 113004 [*Erratum ibid.* **D 61** (2000) 099901] [hep-ph/9906218] [INSPIRE].

[35] E. Accomando, A. Ballestrero, S. Bolognesi, E. Maina and C. Mariotti, *Boson-boson scattering and Higgs production at the LHC from a six fermion point of view: four jets + $\ell\nu$ processes at $\mathcal{O}(\alpha_{EM}^6)$*, *JHEP* **03** (2006) 093 [hep-ph/0512219] [INSPIRE].

[36] A. Ballestrero, G. Bevilacqua and E. Maina, *A complete parton level analysis of boson-boson scattering and electroweak symmetry breaking in $\ell\nu$ + four jets production at the LHC*, *JHEP* **05** (2009) 015 [arXiv:0812.5084] [INSPIRE].

[37] A. Ballestrero, G. Bevilacqua, D.B. Franzosi and E. Maina, *How well can the LHC distinguish between the SM light Higgs scenario, a composite Higgs and the Higgsless case using VV scattering channels?*, *JHEP* **11** (2009) 126 [arXiv:0909.3838] [INSPIRE].

[38] A. Ballestrero, D.B. Franzosi and E. Maina, *Vector-vector scattering at the LHC with two charged leptons and two neutrinos in the final state*, *JHEP* **06** (2011) 013 [arXiv:1011.1514] [INSPIRE].

[39] B. Jager, C. Oleari and D. Zeppenfeld, *Next-to-leading order QCD corrections to W^+W^- production via vector-boson fusion*, *JHEP* **07** (2006) 015 [hep-ph/0603177] [INSPIRE].

[40] B. Jager, C. Oleari and D. Zeppenfeld, *Next-to-leading order QCD corrections to Z boson pair production via vector-boson fusion*, *Phys. Rev.* **D 73** (2006) 113006 [hep-ph/0604200] [INSPIRE].

[41] G. Bozzi, B. Jager, C. Oleari and D. Zeppenfeld, *Next-to-leading order QCD corrections to W^+Z and W^-Z production via vector-boson fusion*, *Phys. Rev.* **D 75** (2007) 073004 [hep-ph/0701105] [INSPIRE].

[42] B. Jager, C. Oleari and D. Zeppenfeld, *Next-to-leading order QCD corrections to W^+W^+jj and W^-W^-jj production via weak-boson fusion*, *Phys. Rev.* **D 80** (2009) 034022 [arXiv:0907.0580] [INSPIRE].

[43] K. Arnold et al., *VBFNLO: a parton level Monte Carlo for processes with electroweak bosons*, *Comput. Phys. Commun.* **180** (2009) 1661 [arXiv:0811.4559] [INSPIRE].

[44] C. Berger et al., *Precise predictions for W + 4 jet production at the Large Hadron Collider*, *Phys. Rev. Lett.* **106** (2011) 092001 [arXiv:1009.2338] [INSPIRE].

[45] T. Han, D. Krohn, L.-T. Wang and W. Zhu, *New physics signals in longitudinal gauge boson scattering at the LHC*, *JHEP* **03** (2010) 082 [arXiv:0911.3656] [INSPIRE].

[46] K.-I. Hikasa and K. Igi, *Strongly interacting WW sector with a scalar resonance*, *Phys. Lett.* **B 261** (1991) 285 [*Erratum ibid.* **B 270** (1991) 128] [INSPIRE].

[47] M.S. Chanowitz and W. Kilgore, *Complementarity of resonant and nonresonant strong WW scattering at the LHC*, *Phys. Lett.* **B 322** (1994) 147 [hep-ph/9311336] [INSPIRE].

[48] A. Dobado, M. Herrero, J. Pelaez and E. Ruiz Morales, *CERN LHC sensitivity to the resonance spectrum of a minimal strongly interacting electroweak symmetry breaking sector*, *Phys. Rev.* **D 62** (2000) 055011 [hep-ph/9912224] [INSPIRE].

[49] J. Oller, *The case of a WW dynamical scalar resonance within a chiral effective description of the strongly interacting Higgs sector*, *Phys. Lett.* **B 477** (2000) 187 [hep-ph/9908493] [INSPIRE].

[50] J. Butterworth, B. Cox and J.R. Forshaw, *WW scattering at the CERN LHC*, *Phys. Rev.* **D 65** (2002) 096014 [hep-ph/0201098] [INSPIRE].

[51] M.S. Chanowitz, *The no-Higgs signal: strong WW scattering at the LHC*, *Czech. J. Phys.* **55** (2005) B45 [hep-ph/0412203] [INSPIRE].

[52] C. Englert, B. Jager, M. Worek and D. Zeppenfeld, *Observing strongly interacting vector boson systems at the CERN Large Hadron Collider*, *Phys. Rev.* **D 80** (2009) 035027 [arXiv:0810.4861] [INSPIRE].

[53] A. Falkowski, C. Grojean, A. Kaminska, S. Pokorski and A. Weiler, *If no Higgs then what?*, *JHEP* **11** (2011) 028 [arXiv:1108.1183] [INSPIRE].

[54] E. Accomando, A. Ballestrero, A. Belhouari and E. Maina, *Boson fusion and Higgs production at the LHC in six fermion final states with one charged lepton pair*, *Phys. Rev.* **D 75** (2007) 113006 [hep-ph/0603167] [INSPIRE].

[55] K. Cheung, C.-W. Chiang and T.-C. Yuan, *Partially strong WW scattering*, *Phys. Rev.* **D 78** (2008) 051701 [arXiv:0803.2661] [INSPIRE].

[56] M.S. Chanowitz, *Strong WW scattering in unitary gauge*, *Phys. Lett.* **B 373** (1996) 141 [hep-ph/9512358] [INSPIRE].

[57] M.S. Chanowitz, *Gauge invariant formulation of strong WW scattering*, *Phys. Lett.* **B 388** (1996) 161 [hep-ph/9608324] [INSPIRE].

[58] A. Alboteanu, W. Kilian and J. Reuter, *Resonances and unitarity in weak boson scattering at the LHC*, *JHEP* **11** (2008) 010 [arXiv:0806.4145] [INSPIRE].

[59] W. Kilian, T. Ohl and J. Reuter, WHIZARD: *simulating multi-particle processes at LHC and ILC*, *Eur. Phys. J.* **C 71** (2011) 1742 [arXiv:0708.4233] [INSPIRE].

[60] A. Ballestrero, A. Belhouari, G. Bevilacqua, V. Kashkan and E. Maina, PHANTOM: *a Monte Carlo event generator for six parton final states at high energy colliders*, *Comput. Phys. Commun.* **180** (2009) 401 [arXiv:0801.3359] [INSPIRE].

[61] J.M. Cornwall, D.N. Levin and G. Tiktopoulos, *Derivation of gauge invariance from high-energy unitarity bounds on the S matrix*, *Phys. Rev.* **D 10** (1974) 1145 [*Erratum ibid.* **D 11** (1975) 972] [INSPIRE].

[62] M.S. Chanowitz and M.K. Gaillard, *The TeV physics of strongly interacting W's and Z's*, *Nucl. Phys.* **B 261** (1985) 379 [INSPIRE].

[63] G. Gounaris, R. Kogerler and H. Neufeld, *Relationship between longitudinally polarized vector bosons and their unphysical scalar partners*, *Phys. Rev.* **D 34** (1986) 3257 [INSPIRE].

[64] S. Weinberg, *Pion scattering lengths*, *Phys. Rev. Lett.* **17** (1966) 616 [INSPIRE].

[65] O. Cheyette and M.K. Gaillard, *The effective one loop action in the strongly interacting standard electroweak theory*, *Phys. Lett.* **B 197** (1987) 205 [INSPIRE].

[66] M.E. Peskin and T. Takeuchi, *A new constraint on a strongly interacting Higgs sector*, *Phys. Rev. Lett.* **65** (1990) 964 [INSPIRE].

[67] M.E. Peskin and T. Takeuchi, *Estimation of oblique electroweak corrections*, *Phys. Rev.* **D 46** (1992) 381 [INSPIRE].

[68] R. Barbieri, A. Pomarol, R. Rattazzi and A. Strumia, *Electroweak symmetry breaking after LEP-1 and LEP-2*, *Nucl. Phys.* **B 703** (2004) 127 [hep-ph/0405040] [INSPIRE].

[69] S. Dawson and G. Valencia, *Bounds on anomalous gauge boson couplings from partial Z widths at LEP*, *Nucl. Phys.* **B 439** (1995) 3 [hep-ph/9410364] [INSPIRE].

[70] O. Eboli, M. Gonzalez-Garcia and J. Mizukoshi, $pp \to jje^{\pm}\mu^{\pm}\nu\nu$ and $jje^{\pm}\mu^{\mp}\nu\nu$ at $\mathcal{O}(\alpha_{EM}^6)$ and $\mathcal{O}(\alpha_{EM}^4\alpha_S^2)$ for the study of the quartic electroweak gauge boson vertex at CERN LHC, *Phys. Rev.* **D 74** (2006) 073005 [hep-ph/0606118] [INSPIRE].

[71] J. van der Bij and B.M. Kastening, *Corrections to oblique parameters induced by anomalous vector boson couplings*, *Phys. Rev.* **D 57** (1998) 2903 [hep-ph/9708438] [INSPIRE].

[72] M. Fabbrichesi and L. Vecchi, *Possible experimental signatures at the CERN LHC of strongly interacting electro-weak symmetry breaking*, *Phys. Rev.* **D 76** (2007) 056002 [hep-ph/0703236] [INSPIRE].